Faculdade de Engenharia da Universidade do Porto

Silicon Photonics Optical Beamformer for Broadband Phased Array Antennas

David Miguel Nunes Cunha

Mestrado Integrado em Engenharia Eletrotécnica e de Computadores

Supervisor: Professor Henrique Manuel de Castro Faria Salgado

Co-Supervisor: Dr. Bilal Hussain

July 27, 2021

Abstract

This dissertation project proposes the design of a Silicon Photonics Optical Beamformer for Broadband Phased Array Antennas operating in the Ka band (26 - 40 GHz). The beamformer circuit implements a True Time Delay device, that enables seamless tuning of a flat time delay for each radiating element, which produces a phase shift that varies linearly with frequency over the entire signal bandwidth. The linear frequency dependence of the generated phase shifts eliminates a recurring phenomenon on PAA systems known as beamsquint, which consists in deformation of the array radiation pattern that deteriorates the quality of the transmitted signal. Therefore this technology allows PAA based systems to be used in broadband communications, which are becoming evermore pervasive, due to modern day demands for high-speed data transfer.

Acknowledgements

I would like to thank:
Professor Henrique Salgado for supervising my dissertation work.
Dr. Bilal Hussain for his help and expertise conveyed throughout the project.

My parents and my sister for the constant support they provided in every step of my life.
Finally, I would like to thank my grandfather Álvaro for inspiring me to stay curious.

David Cunha

"If people do not believe that mathematics is simple,
it is only because they do not realize how complicated life is."

John von Neumann

Contents

1 Introduction **1**
- 1.1 Objectives . . . 1
- 1.2 Background and Motivation . . . 1
- 1.3 Project Contributions . . . 2
- 1.4 Document Structure . . . 3

2 State of the Art **5**
- 2.1 Introduction . . . 5
- 2.2 Phased Array Antennas . . . 5
  - 2.2.1 Antenna Array Theory . . . 5
  - 2.2.2 Beam Scanning systems . . . 7
- 2.3 Photonic Integrated Circuits . . . 8
  - 2.3.1 Modelling and Simulation Tools . . . 8
  - 2.3.2 Waveguides . . . 9
  - 2.3.3 Directional Couplers . . . 12
  - 2.3.4 Mach–Zehnder interferometer . . . 13
  - 2.3.5 Multi-mode Interference Couplers . . . 15
  - 2.3.6 Grating Couplers . . . 18
- 2.4 Optical Ring Resonators . . . 19
  - 2.4.1 Fundamental properties of ring resonators . . . 19
  - 2.4.2 Resonance wavelength tuning . . . 22
  - 2.4.3 Applications of ring resonators . . . 23
- 2.5 PIC Beamformer Implementations . . . 24
- 2.6 Summary . . . 25

3 Delay Unit Design **27**
- 3.1 Introduction . . . 27
- 3.2 Device Specifications . . . 27
- 3.3 Ring Resonator Spectral Characteristics . . . 28
  - 3.3.1 Transmission and Free Spectral Range . . . 28
  - 3.3.2 Group Delay Response . . . 32
- 3.4 Group Delay Amplitude Control . . . 36
  - 3.4.1 Variable Coupler . . . 36
  - 3.4.2 Amplitude Range and Resolution . . . 40
- 3.5 Resonance Wavelength Tuning . . . 43
  - 3.5.1 Design and Validation . . . 43
  - 3.5.2 Delay Bandwidth . . . 45
- 3.6 Bend Waveguide . . . 46

3.6.1 Bend Losses . . . 46
3.6.2 Validation . . . 48
3.7 Summary . . . 48

4 Numerical Simulations **51**
4.1 Introduction . . . 51
4.2 Delay Unit Simulation Results . . . 51
4.3 Modulation and Demodulation . . . 55
4.3.1 Intensity Modulation . . . 55
4.3.2 Single-Sideband Suppressed Carrier Modulation . . . 59
4.4 Summary . . . 61

5 Beamformer **63**
5.1 Introduction . . . 63
5.2 Array Antenna . . . 63
5.2.1 Linear Array Model . . . 63
5.2.2 Progressive phase shift . . . 63
5.3 System Architecture . . . 65
5.4 Layout Development . . . 66
5.4.1 Input/Output Coupling . . . 66
5.4.2 Delay Unit . . . 66
5.4.3 Electric contacts . . . 69
5.5 Summary . . . 69

6 Final Remarks **71**
6.1 Goal Achievement . . . 71
6.2 Future Work . . . 72

List of Figures

2.1 Far field geometry of N-element array of isotropic sources [1] . . . 6
2.2 Incremental switched line [2] . . . 7
2.3 Original Rotman Lens Architecture Diagram [3] . . . 8
2.4 Overview of a silicon photonic system design workflow [4] . . . 9
2.5 Cross-section of SOI wafer[4] . . . 10
2.6 Strip waveguide (left); rib waveguide (right)[4] . . . 10
2.7 Cross section of rectangular waveguide [5] . . . 11
2.8 E-field intensity of 2D mode profile simulation on a strip waveguide [4] . . . 11
2.9 Conventional directional coupler [6] . . . 12
2.10 Y-branch splitter . . . 13
2.11 Y-branch combiner . . . 13
2.12 Single-mode Y-branch diagram [7] . . . 14
2.13 Mach-Zender diagram . . . 15
2.14 Multi-mode interferometer diagram [8] . . . 15
2.15 The optical Talbot effect for a monochromatic light, known as 'Talbot Carpet' [9] . . . 16
2.16 Input field $\Phi(y, 0)$ replicas in multimode waveguide [10] . . . 18
2.17 schematic of a cross section of a grating couple [11] . . . 18
2.18 Diagram of racetrack resonators: All-pass (left) and Add-drop (right) [4] . . . 19
2.19 Simulated response of a Add-drop ring resonator for the through- (black) and drop port (grey). Also shown is the Free Spectral Range, the distance between two consecutive fringes. At the right simulated fields of the MR are given; top: ON resonance, Bottom: OFF resonance [12] . . . 22
2.20 Ring resonator group delay, for different values of cross-over coupling coefficient [13] . . . 24
2.21 Ring resonator group delay response of three cascaded ORR [13] . . . 24
2.22 Diagram of the 3-stage ring resonator filter [14] . . . 25

3.1 Single All-pass ORR schematic . . . 29
3.2 Transmission Phase . . . 30
3.3 Transmission response plot (Real part) . . . 30
3.4 All-pass ORR with PDK components . . . 31
3.5 Transmission magnitude response (blue: ideal components/ green: PDK components) . . . 31
3.6 All-pass ORR group delay response . . . 32
3.7 Theoretical delay model plot . . . 32
3.8 ORR Group delay response as a function of coupling coefficient (blue: 0.5; green: 0.7; red: 0.9) . . . 33

3.9 Theoretical model as a function of coupling coefficient (blue: 0.5; orange: 0.7; yellow: 0.9) . . . 33
3.10 All-pass ORR with phase shifter . . . 34
3.11 ORR Group delay as a function of round trip phase (blue: 0; green: $\frac{\pi}{4}$; red: $\frac{\pi}{2}$; purple: $\frac{3\pi}{4}$) . . . 34
3.12 Theoretical model of the group delay as a function of round trip phase (blue: 0; orange: $\frac{\pi}{4}$; yellow: $\frac{\pi}{2}$; purple: $\frac{3\pi}{4}$) . . . 35
3.13 3 cascaded ORR, with incremental round-trip phases . . . 35
3.14 3 cascaded ORR group delay response . . . 36
3.15 GDS layout of directional coupler developed for this project . . . 37
3.16 Variable coupler diagram and working modes [15] . . . 38
3.17 cross-over coupling power gain as function of coupling length . . . 39
3.18 cross-over coupling power gain for $L = 5.35\,\mu m$ and operation wavelength $\lambda = 1550\,nm$ . . . 39
3.19 PDK Directional Coupler analysis schematic . . . 39
3.20 Phase shifter Interconnect block . . . 40
3.21 Variable Coupler schematic . . . 40
3.22 cross-over coupling power gain as a function of phase shifter bias . . . 41
3.23 ORR connected to Variable Coupler . . . 42
3.24 Group Delay Response Plot . . . 42
3.25 Delay unit with resonance frequency tuning . . . 44
3.26 Plot of group delay response as a function of ring phase shifter bias voltage . . . 44
3.27 Bend 3D model . . . 47
3.28 E-field intensity . . . 47
3.29 Delay Unit schematic with bends . . . 48

4.1 Amplitude as a function of V1 . . . 52
4.2 Resonance Frequency as a function of V1 . . . 52
4.3 Resonance Frequency as a function of V2 . . . 53
4.4 Amplitude as a function of V2 . . . 53
4.5 Amplitude as a function of V1 + polynomial approximation . . . 55
4.6 Amplitude as a function of V2 + polynomial approximation . . . 55
4.7 MZM response to bias voltage sweep . . . 56
4.8 MZM schematic . . . 57
4.9 MZM output signal . . . 57
4.10 Spectrum of modulated signal. The dotted line describes the necessary delay bandwidth [13]. . . . 57
4.11 Delay Unit with two cascaded rings . . . 58
4.12 Delay Unit response . . . 58
4.13 Electric signals after photodetector demodulation . . . 59
4.14 Spectrum of modulated signal after carrier and sideband suppression. The dotted line describes the necessary delay bandwidth [13]. . . . 60
4.15 MZM based Intensity Modulation with SSB-SC . . . 60
4.16 Before the photodetector, the Delay Unit output is combined with the optical carrier . . . 60
4.17 Electric signals after the photodetector detected by the oscilloscope . . . 61

5.1 Phased Antenna Array Diagram . . . 64
5.2 Broadside Antenna Array Diagram . . . 64

5.3 Beamformer Architecture Diagram 66
5.4 Beamformer Photonic Chip Layout 67
5.5 Grating Coupler Fibre Array 67
5.6 Single Adiabatic Bend Layout 67
5.7 Double Adiabatic Bend Layout 67
5.8 MMI 1×4 splitter 68
5.9 Delay Unit Layout 68
5.10 Delay Unit Electrical Connections and Bondpads 69
5.11 Taper Example Layout 69

Abbreviations and symbols

AE	*Antenna Elements*
FDTD	*Finite Difference Time Domain*
FSR	*Free Spectral Range*
FWHM	*Full Width at Half Maximum*
MZI	*Mach-Zender interferometer*
MZM	*Mach-Zender modulator*
MMIC	*Monolithic Microwave Integrated Circuit*
MMI	*Multi-mode Interference*
ONA	*Optical Network Analyser*
ORR	*Optical Ring Resonator*
PAA	*Phased Array Antennas*
PDK	*Process Design Kit*
PIC	*Phtonic Integrated Circuit*
SOI	*Sillicon-on-insulator*
TTD	*True Time Delay*

λ	Wavelength
β	Phase constant
τ	Group Delay

Chapter 1

Introduction

1.1 Objectives

The aim of this project is to design and simulate a Photonic Integrated Circuit (or PIC) optical beamformer for broadband phased array antennas operating in the K_a band (26 - 40 GHz). The beamformer circuit should implement seamless tunable true time delay for each Antenna Element (AE). The optical beamformer to be designed is intended for satellite communication applications.

1.2 Background and Motivation

Phased Array Antennas (PAA) consist of multiple stationary radiating elements, commonly referred to as antenna elements (AEs), which are capable of steering the maximum radiation, by controlling the progressive phase difference between the AEs [1]. This feature, called beam steering, is of great interest, because it means the antenna beam can be controlled electronically, without requiring the AEs to physically move. It is also possible to provide variable amplitude control for radiation pattern shaping, for example to minimise side lobes [16][13]. PAA were introduced in the early 20th century and developed extensively during World War II, mainly for radar systems [16]. Nowadays, PAA based systems have countless applications, such as radar, satellite communication, space probe communications [17] and weather monitoring.

A PAA system also requires a *beamformer*, that is responsible for the shaping of the beam, which is achieved by controlling the amplitude and phase of the excitation current in the AEs. Classical PAA beamformers use *phase shifters* in order to induce a tunable phase to the signal of the AEs, hence controlling the direction of maximum radiation of the antenna array beam. The phase shift introduced by phase shifters at a sub-array level is not linearly frequency dependent. This means that for different frequencies correspond different time delays, which

results in distortion of the beam over frequency, known as *beam squinting*, thus severely reducing the bandwidth of the PAA [18]. As a consequence, this conventional approach works well for narrow band applications, but it does not constitute a viable solution for broadband communications.
It is therefore increasingly more relevant to develop PAA beamformers for broadband communications, in order to meet current and future needs in data transfer. This is especially important in satellite communication systems, which involve fast moving transmission/reception targets (namely in low orbits) used for broadband communication, such as those providing broadband internet service, like *Star Link* [19]. Beam squinting, which is the biggest impediment to broadband PAA beamforming, can be eliminated by replacing the phase shifters with TTD devices. However, TTD devices require continuous delay tuning in order to achieve high beam angle resolution [13], which is not feasible to implement electronically. Thus, an optical beamformer based in Optical Ring Resonators (ORR) is proposed in this work as a solution to address this issue.
Traditional approaches of beamformers based on electronics be it analogue in nature or digital have various limitations, especially if the signal bandwidth is large. Hence, the proposed solution based on photonic circuits, a technology which is evolving quite rapidly, presents a very attractive solution to solve the present needs of high data rates [4]. This technology has applications on 5G wireless communications as well as high data rate satellite communications for internet service provision.

1.3 Project Contributions

The general structure of the proposed optical beamformer can be described as a network of tunable delay lines based on ORR. It is largely based on the solutions proposed by [13] [14]. However, some of the details and components regarding the design and implementation of the device were adapted from other sources or entirely developed from scratch:

- The variable coupler design (see section 3.4.1), which is based on a *Mach-Zender Interferometer tunable coupler* implementation proposed by [20] [15] and adapted to optical beamforming applications.
- The development of modular delay units, which constitute a highly scalable design for larger phased arrays, requiring only the incorporation of more delay units and the respective calibration.
- The group delay response resonance frequency tuning via a thermo-optic phase shifter.
- Numerical simulations and validation of the delay unit operation.
- The overall beamformer architecture development. The beamformer proposed in this dissertation constitutes a device that enables high precision beamsteering for broadband signals, which is not limited by beamsquint.

In short, the proposed solution is based on a concept that has already been studied in detail by many authors, nevertheless, the specific architecture proposed constitutes a novel approach for optical beamformers based on tunable delay lines.

1.4 Document Structure

This document is divided into 6 chapters. Chapter 1 presents the objectives for this project, the background and motivation and the project contributions, which contextualise the project within the state-of-the-art of optical beamforming. Chapter 2 contains an overview of the state-of-the-art in photonic integrated technology, the associated optical components as well as some of the theoretical fundamentals in those said components and Phased Array Antennas. Chapter 3 presents a detailed description of the design process for the Delay Unit, which constitutes the most important component in the beamformer architecture. Chapter 4 describes the numerical simulations performed, and the corresponding results, in order to validate the Delay Unit and present a detailed characterisation of the device response. Chapter 5 presents the beamformer architecture and the relevant topics concerning the system overall design, i.e., from the array antenna model to the final PIC layout. Finally, Chapter 6 contains the final remarks regarding the project's overall success. Additionally, a list of suggestions for future development are outlined.

Chapter 2

State of the Art

2.1 Introduction

In this Chapter, a State of the Art review on Phased Array Antennas (PAA), integrated photonics technology and the most relevant optical components concerning this project is presented. Section 2.2 presents and overview of the fundamentals in Phased Array Antennas, as well as some implementations for beam scanning systems. Subsequently, in Section 2.3 a state-of-the-art review in Silicon Photonics technologies and the most relevant optical components was outlined. Finally, Section 2.4 is dedicated to Optical Ring Resonators, as they constitute the most important aspect for the beamformer design.

2.2 Phased Array Antennas

Since the optical circuit designed will function as a delay scanning device for beam direction control of a Phased Array Antenna, it is relevant to present an overview of the fundamentals of these devices.

2.2.1 Antenna Array Theory

Considering an N-element linear array, i.e. an antenna made up of N discrete elements with a geometry as described in Figure 2.1, let us assume that all elements have identical amplitudes and a constant β progressive phase lead current excitation relative to the preceding one (β represents the phase by which the current in each element leads the current of the preceding element). An array with these conditions is named a *uniform array*. If we sum the electric fields of all elements, we obtain a total field that is equal to the field of a single element positioned at the origin multiplied by a factor referred to as *Array Factor*. The array factor is a function of the number of elements, their geometry, relative phase, magnitude and spacing [1]. Since the array factor is independent of the directional characteristics of the elements' fields, it can be obtained by considering the elements as isotropic point sources. The array

factor is given by [1]:

$$AF = \sum_{n=1}^{N} e^{j(n-1)\psi} \quad \text{where } \psi = kd\cos\theta + \beta \tag{2.1}$$

If the actual elements are not isotropic sources, the total field can be calculated by multiplying

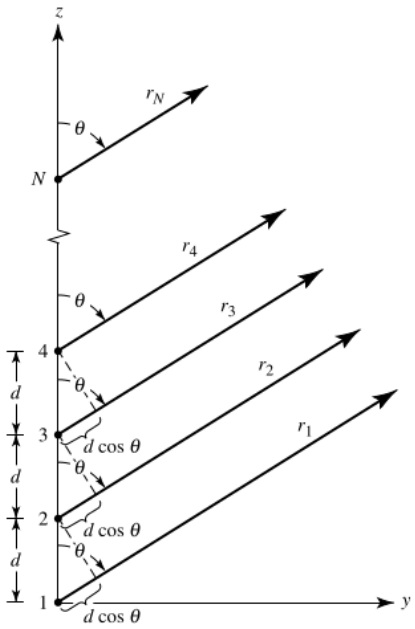

Figure 2.1: Far field geometry of N-element array of isotropic sources [1]

the array factor by the field of a single element, referred to as *element factor*. From Equation 5.1, it is possible to write the array factor as a function of ψ, as follows (see [1] for detailed explanation):

$$AF = \frac{\sin(\frac{N}{2}\psi)}{\sin(\frac{1}{2}\psi)} \tag{2.2}$$

which, for small values of ψ can be approximated to:

$$AF = \frac{\sin(\frac{N}{2}\psi)}{\frac{\psi}{2}} \tag{2.3}$$

From this relation, it follows that the array factor function has a period of 2π and the maximum and nulls of the array factor are dependent on the distance d between the array elements and the progressive phase shift β. Thus, by controlling the phase excitation between the elements, it is possible to direct the maximum radiation of on array in any desired direction to form a scanning array. This is the principle of electronic scanning phased array operation [1].

2.2.2 Beam Scanning systems

In order to have a continuous scanning of the array radiation beam, the system should be capable of varying the progressive phase between the elements. In practice this is accomplished electronically by the use of ferrite or diode phase shifters. An example of a diode phase shifter is an *incremental switch-line*, as shown in Figure 2.2. This device works by switching on an off the lines of lengths l_1 and l_2. The differential phase shift (in degrees) is given by:

$$\Delta\phi = k(l_2 - l_1) \tag{2.4}$$

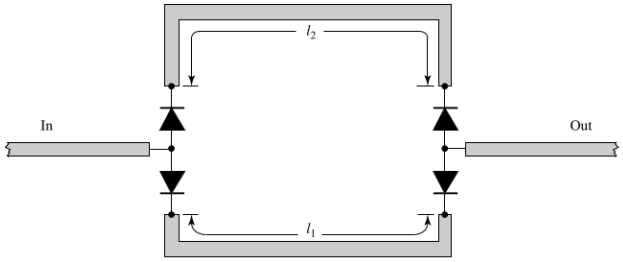

Figure 2.2: Incremental switched line [2]

As mentioned in section 1.2, the phase shifts implemented by these circuits to not follow a linear variation with frequency, which will cause the beam to widen in broadband applications, known as *beamsquinting*. This is one of the main issues the proposed solution of this project intends to overcome.

Another implementation of an electronic beam scanning system is known as a *rotman lens*. The Rotman lens consists of two geometric contours where excitation of a feed at a beam port along contour 1 will produce a linear phase front at the element ports, corresponding to a given direction. Reciprocally, in receive, a wavefront which arrives with proper phase at the element ports will be focused at the corresponding beam-port [18]. Figure 2.3 depicts the original architecture for a Rotman Lens. Antenna elements are connected to the right side as depicted in Figure 2.3, with beam ports connected to the left. The lens can be thought of as a quasi-microstrip (or quasi-stripline) circuit where the beam ports are positioned such that constant phase shifts are achieved at the antenna ports. When antenna elements are fed at phases that vary linearly across a row, it behaves just like a phased array.

Other, more advanced, techniques have been used in order to implement True Time Delay Devices, namely in electronic integrated circuits for microwave applications, such as MMIC (*Monolithic Microwave Integrated Circuit*). A full review of these implementations is beyond the scope of this dissertation and, thus, will not be included in the present document.

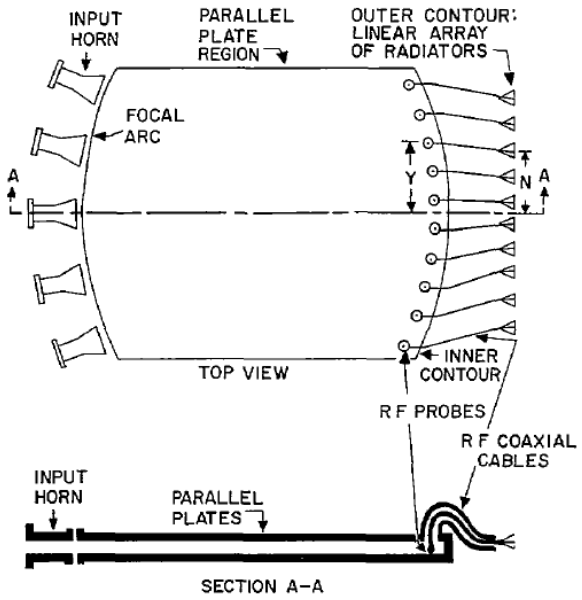

Figure 2.3: Original Rotman Lens Architecture Diagram [3]

2.3 Photonic Integrated Circuits

Photonic Integrated Circuits (PIC) are a fast growing field, both academically and in industry development. The ability to integrate optical components such as waveguides, ring resonators, lasers and photodiodes in a single chip will likely make this technology ubiquitous worldwide within the near future [4]. PIC can be of use in various fields from high-speed communications, to sensor systems and medical applications. This is especially true for Silicon Photonics. Furthermore, there has been a great effort in order to repurpose process steps, materials and techniques used and developed over the past 50 years in the fabrication of silicon microelectronics to build silicon photonic devices and circuits [4].
This section contains an overview of the state of art of the most relevant optical devices related to this project as well as an explanation on their working principles and applications.

2.3.1 Modelling and Simulation Tools

Regarding Silicon Photonics, it is important for this project to grasp how the design process of PIC is conducted. The design workflow for a photonic system is presented in Figure 2.4.

Firstly, mathematical models and techniques must be employed in order to calculate important parameters that characterise the behaviour of photonic systems. An example is the eigenmode solver, which determines time-harmonic solutions to Maxwell's equations in the frequency domain. There are numerous approaches to solving this problem, including the Finite Element Method, Finite Difference and various approximations, such as the Effective Index Method. The design of photonic devices also requires an understanding of how light propagates in a waveguide. The most general and rigorous time-domain approach is the finite

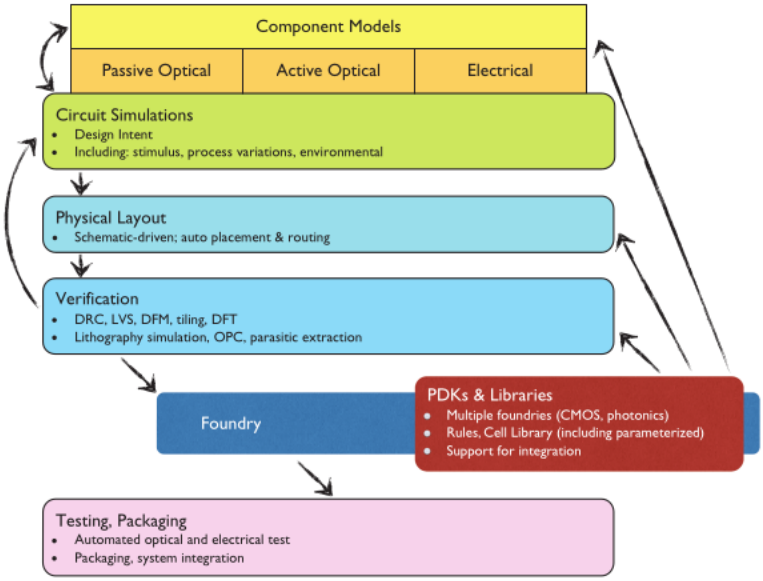

Figure 2.4: Overview of a silicon photonic system design workflow [4]

difference time domain method (FDTD).
With these models, simulation software (like *Lumerical*) can be developed and used to simulate the response of various devices to predict the system behaviour in the presence of external stimulus, namely electrical and optical signals. Once a circuit is designed, a designer uses the schematic to lay out the components in a physical mask layout, using a variety of design aids and component libraries, such as Process Design Kits (PDK). This is followed by verification, including manufacturing design rule checking, layout versus schematic (LVS), lithography simulation and parasitic extraction. In this step, fabrication processes and environmental variations are also taken into consideration [4].

2.3.2 Waveguides

Optical waveguides are devices designed to confine and guide light through a well defined path. Before considering waveguide behaviour, it is relevant to analyse what materials are used for implementing waveguides in photonic circuits, namely silicon photonics, which is the technology that will be used for this project.

2.3.2.1 Silicon-on-insulator

The wafers commonly used for silicon photonics are called 'silicon-on-insulator' (SOI), which are also commonly used in the electronics industry for high-performance circuits. They consist of overlapping layers of silicon and silicon oxide. The typical 200 mm (8") wafer consists of a 725 µm silicon substrate, 2 µm of oxide (buried oxide, or BOX), and 220 nm of crystalline

silicon [4], as described in Figure 2.5. The refractive index in Silicon is temperature depen-

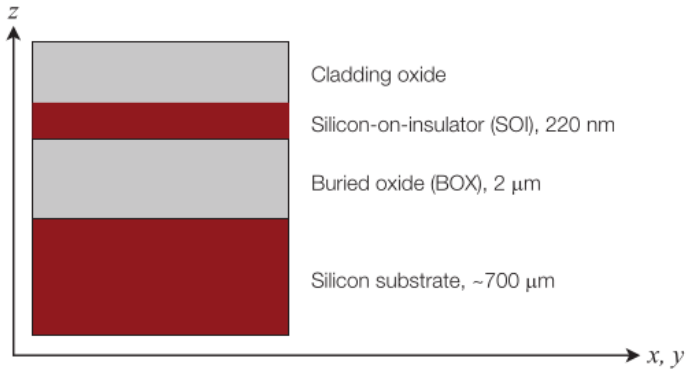

Figure 2.5: Cross-section of SOI wafer[4]

dant. This dependence is caused by the modification in the distribution function of carriers and photons, and the temperature induced shrinkage of the band gap [4]. The direction of the temperature change can be sensed by exploiting variations in wafer thickness [21]. The temperature dependence can be approximated by $\beta(T) = \frac{1}{n}\frac{dn}{dT}$, which for silicon is $5.2 \cdot 10^{-5} K^{-1}$ and $\frac{dn}{dT} = 1.87 \cdot 10^{-4} K^{-1}$ at 1500 nm. This behaviour of silicon based waveguides will be very useful for thermally tuned devices, see section 2.4.2.

2.3.2.2 Waveguides

There are two common types of waveguides used in silicon photonics: *strip waveguides*, typically used for routing and the *rib waveguides* used for electro-optic devices such as modulators, since it enables electrical connections to be made to the waveguide [4]. These are represented in Figure 2.6. In order to properly design an optical waveguide, one must take into consider-

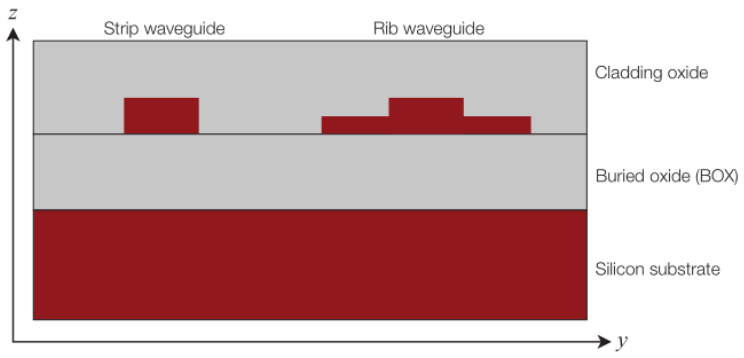

Figure 2.6: Strip waveguide (left); rib waveguide (right)[4]

ation mode propagation. This aspect is the most relevant when designing waveguides, thus simulations are performed in order to determine the proper dimensions, namely the silicon

layer width and height, based on certain requirements e.g., the waveguide should only support a single TM and TE mode. The waveguide height (which corresponds to the silicon layer thickness) is typically constrained by the foundry. To determine the mode field configuration, one must find the *eigenvalue* for each mode. Analysing the mode structure of a dielectric involves extensive calculations (see [5] for more details), but, for a rectangular waveguide, it can be shown that the critical cut-off condition will be determined by the smaller of the two dimensions (a and b) of the waveguide (see Figure 2.7). The normalised frequency corresponds to an upper limit, hence only modes that occur at lower normalised frequency values can propagate in the waveguide. This is defined as [5]:

$$V = k_0 \frac{a}{2} \sqrt{n_1^2 - n_2^2} \tag{2.5}$$

Where a is the smaller dimension, k_0 is the free space *wavenumber*, n_1 is the core refractive index and n_2 is the index of the surrounding material. As an example, it is shown in fig 2.8 the

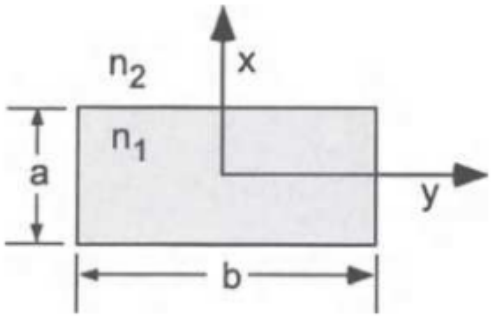

Figure 2.7: Cross section of rectangular waveguide [5]

results of a mode profile simulation, for the first TE mode profile of a 500 nm × 220 nm strip waveguide at 1550 nm. Similarly to circular waveguides, in rectangular waveguides, modes

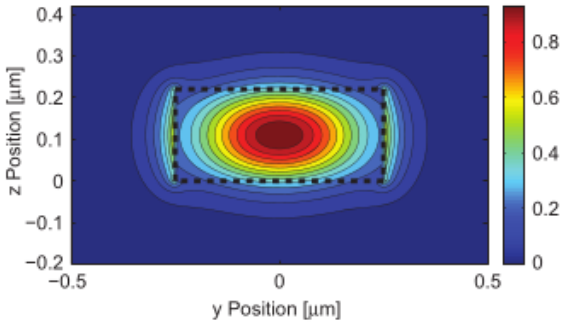

Figure 2.8: E-field intensity of 2D mode profile simulation on a strip waveguide [4]

will decay exponentially in the cladding, proportionally to distance. The decay of the field

profile can be approximated by:

$$E \propto e^{-\frac{2\pi d}{\lambda}} \sqrt{n_{eff} - n_c^2} \tag{2.6}$$

where E is the field amplitude at a distance d from the core-cladding interface, n_{eff} is the effective index of the mode, and n_c is the refractive index of the cladding. The mode effective index can be calculated as $n_{eff} = \frac{\beta}{k_0}$, where β is the propagation coefficient [5].
Optical waveguides, like all passive components, are subjected to losses and this aspect should also be taken into consideration while designing an optical circuit. Losses in waveguides can stem from several factors, such as:

- Absorption due to metal proximity;
- Sidewall roughness can cause optical scattering loss, resulting from roughness of the waveguide surface, which is one of the main sources of optical propagation loss [22]. Consequently, there has been much research in this area in order to better model the relation between propagation losses and sidewall roughness;
- Material Loss;
- Bend losses, which are introduced by the use of bent waveguides.

2.3.3 Directional Couplers

Directional couplers are the most common method for combining and splitting light in photonic systems. This component is used for various purposes, such as splitting a portion of light into ring resonators or for coupling two inputs in fibre interferometers. The directional coupler consists of two parallel waveguides, where the coupling coefficient is controlled by the length of the coupler and the spacing between the two waveguides [4], see Figure 2.9.
The behaviour of directional couplers can be derived from coupled mode theory [6]. Consid-

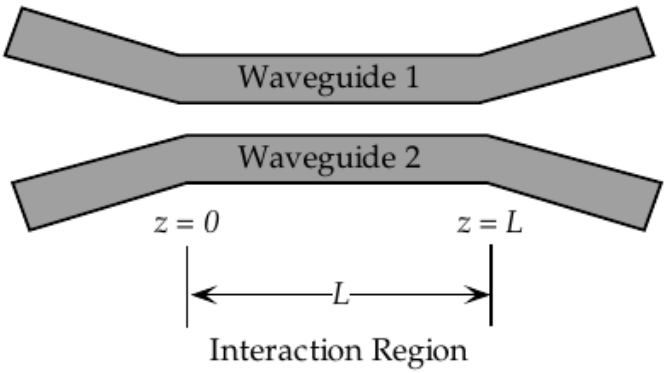

Figure 2.9: Conventional directional coupler [6]

ering the conventional configuration of directional couplers (Figure 2.9), the fraction of the power coupled from one waveguide to the other, k, can be expressed as:

$$k^2 = \frac{P_{cross}}{P_0} = \sin^2(CL) \tag{2.7}$$

Where P_0 is the input optical power, P_{cross} is the power coupled across the coupler into the other waveguide, L is the length of the coupler and C is the coupling coefficient. The remaining fraction of power in the original waveguide is:

$$t^2 = \frac{P_{thru}}{P_0} = \cos^2(CL) \tag{2.8}$$

It should be noted that for a lossless coupler, the following relation must be satisfied $t^2 + k^2 = 1$. By decomposing the propagation light field into the modes at that position (known as 'supermodes', see *Eigenmode Expansion Method*), the coupling coefficient can be obtained based on a numerical calculation of the effective indices n_1 and n_2, which correspond to the first two eigenmodes of the coupled waveguides. From these two supermodes, the coupling coefficient is described by the following expression:

$$C = \frac{\pi \Delta n}{\lambda} \tag{2.9}$$

where Δn is the difference between the effective indices, $n_1 - n_2$.
In Silicon Photonics, directional couplers can be implemented using either strip or rib waveguides [4].

2.3.4 Mach–Zehnder interferometer

Before explaining what it is and how a Mach-Zender interferometer works, it is important to consider the operation of Y-branches. Y-branches are devices used to split light from one waveguide equally into two output branches or to combine light from two input branches into one waveguide, as represented in Figures 2.10 and 2.11. The splitting functionality analysis is

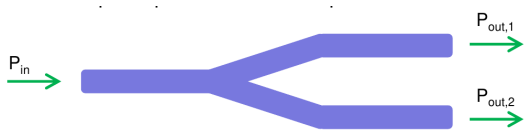

Figure 2.10: Y-branch splitter

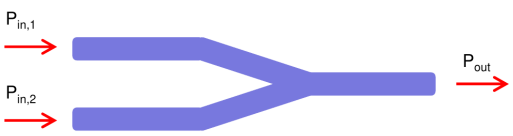

Figure 2.11: Y-branch combiner

quite straightforward, as for an input field intensity I_{in}, the intensity in each output branch will be $I_1 = I_2 = I_{in}/2$, and consequently the electric field $E_1 = E_2 = E_{in}/\sqrt{2}$. For the combiner, the analysis is not as simple, as the y-branch cannot be considered as a three-port device.
According to [7], the Y-junction will be treated as three single mode waveguides. A symmetric

structure of three identical waveguides is assumed, where three sections can be identified Figure 2.12. The branching section smoothly terminates two waveguides into one. The tapered section consists of a waveguide with varying width along the propagation direction. The two incident light waves are assumed to be completely coherent and monochromatic, thus having the same frequency and a constant phase difference.
When the input modes are in phase, the output power will result in the sum of the input powers, because the even mode will be excited, which is converted into the fundamental mode and successfully confined in the output waveguide. On the other hand, if the two incoming waves are opposite in phase, no guided mode will be confined in the output waveguide, because the odd mode will be excited, which is converted into the evanescent mode, decreasing exponentially as it passes through the tapered section. If a light beam is only incident from one waveguide, even and odd modes will be equally excited, which will result in a 3 dB insertion loss, since the power of the odd mode is lost in the tapered section. The transmission

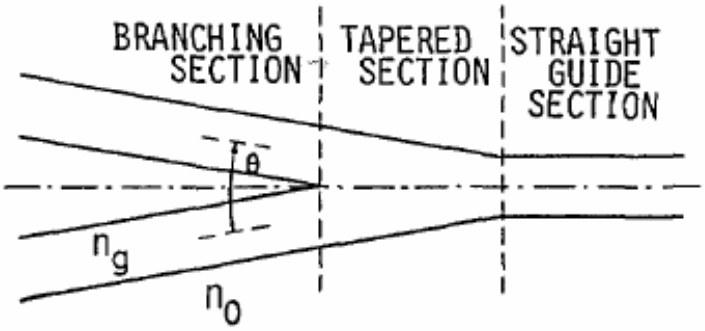

Figure 2.12: Single-mode Y-branch diagram [7]

matrix for the Y-branch splitter and combiner are, respectively, as follows:

$$\begin{pmatrix} E_{out,1} \\ E_{out,2} \end{pmatrix} = \begin{pmatrix} \frac{\sqrt{2}}{2} e^{-j\theta} \\ \frac{\sqrt{2}}{2} e^{-j\theta} \end{pmatrix} E_{in} \tag{2.10}$$

$$E_{out} = \begin{pmatrix} \frac{\sqrt{2}}{2} e^{-j\theta} & \frac{\sqrt{2}}{2} e^{-j\theta} \end{pmatrix} \begin{pmatrix} E_{in,1} \\ E_{in,2} \end{pmatrix} \tag{2.11}$$

A Mach–Zehnder interferometer consists of a device that splits an input light wave into two beams that are recombined at the output. Simply put, it consists of two symmetrical single-mode Y-branches connected to arms with different optical lengths, represented in Figure 2.13. In optical fibre communications, these devices can be used, among other applications, to modulate the power or phase of a laser beam. Considering Y-branch splitter and combiner transmission matrices 2.10 and 2.11 and considering that the two propagating lines introduce a phase delay of $e^{-j\phi_i}$, where $\phi_i = \beta_i L_i$ and L_i is the line length, it is possible to relate the

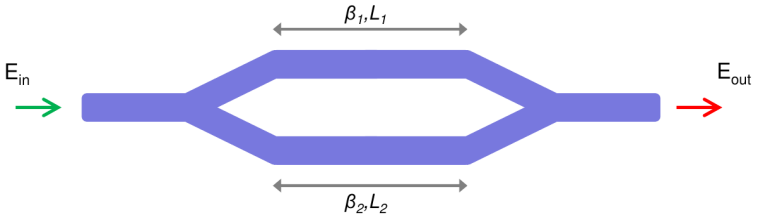

Figure 2.13: Mach-Zender diagram

input and output field waves as described:

$$E_{out} = \begin{pmatrix} \frac{\sqrt{2}}{2}e^{-j\theta} & \frac{\sqrt{2}}{2}e^{-j\theta} \end{pmatrix} \begin{pmatrix} e^{-j\phi_1} & 0 \\ 0 & e^{-j\phi_2} \end{pmatrix} \begin{pmatrix} \frac{\sqrt{2}}{2}e^{-j\theta} \\ \frac{\sqrt{2}}{2}e^{-j\theta} \end{pmatrix} E_{in} \tag{2.12}$$

From 2.12, it follows that:

$$P_{out} = \cos^2(\frac{\Delta\phi}{2})P_{in} = \cos^2(\frac{\beta_2 L_2 - \beta_1 L_1}{2})P_{in} \tag{2.13}$$

Consequently, the output power of the interferometer is a sinusoidally varying function of wavelength (via β_1 and β_2) for an imbalanced interferometer ($L_1 \neq L_2$).

2.3.5 Multi-mode Interference Couplers

Multi-mode interference (MMI) couplers consists essentially of a broad multimode waveguide, which supports a large number of modes. This section has several access waveguides connected, as shown in Figure 2.14. MMI based devices enable optical signal routing, as they can perform splitting and combining functions. Multi-mode interference couplers are based on the

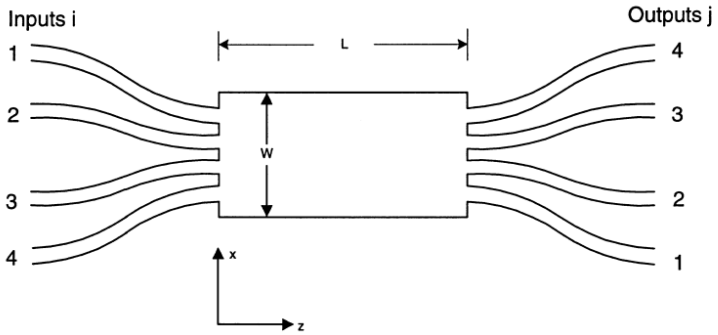

Figure 2.14: Multi-mode interferometer diagram [8]

self-imaging property of multi-mode propagation in a slab waveguide [8]. This phenomenon, also known as the *Talbot effect*, describes the lens-less self-imaging of a grating by diffraction in the optical near-field, as exemplified in Figure 2.15. When a monochromatic wave falls onto a grating it generates self-images of the grating pattern at regular intervals of nL_T, where L_T

is known as the *Talbot Distance* [9]. The Talbot Length L_T depends on the wavelength λ and the grating period Λ, defined by *Lord Raleigh* as follows:

$$L_T = \frac{\lambda}{1 - \sqrt{1 - (\frac{\lambda}{\Lambda})^2}} \tag{2.14}$$

He also suggested a simplified version of 2.14, valid when the wavelength λ is considered to be small compared to Λ. In this approximation, the Talbot Length can be described as[23]:

$$L_T = \frac{2\Lambda^2}{\lambda} \tag{2.15}$$

It is also worth mentioning that the self-images that occur in even n multiples of the Talbot Length are shifted by half a period compared to the images with odd n, as shown in Figure 2.15. Based on this property, MMI couplers are able to couple light to multiple output ports

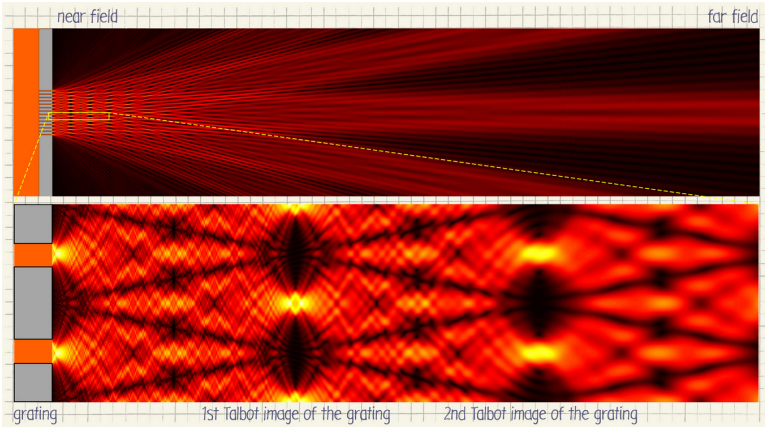

Figure 2.15: The optical Talbot effect for a monochromatic light, known as 'Talbot Carpet' [9]

and function as splitter or combiner, by specifying a given width W and length L for the central section, as shown in Figure 2.14. This phenomenon is a result of interactions inside the multimode waveguide between the multiple modes excited by the input field, which is described with greater rigour in the following paragraphs.

The central section of an MMI device is a waveguide designed to support a large number of modes (typically ≥ 3). In order to launch and recover light from that waveguide, a number of access waveguides (usually single-mode) are placed at its input and output. Hence, such devices can be referred as *NxM MMI couplers*, where N and M are the number of input and output waveguides, respectively [10]. The effective index method may be applied to reduce the description of the modes from two to one dimension. The input field $\Phi(x, 0)$, is written

as a sum of the slab modes, $\phi(x)$, as follows:

$$\Phi(x,0) \approx \sum_{m=0}^{M-1} C_m \phi_m(x) \tag{2.16}$$

where C_m represents the amplitude of the mth waveguide, which is defined in terms of the overlap integral[1]:

$$C_m = \frac{\int \Phi(x)\phi_m(x)dx}{\sqrt{\int \phi_m(x)^2 dx}} \tag{2.17}$$

This is known as eigenmode decomposition, where the $\phi_m(x)$'s are the eigenmodes of the slab waveguide. The field as it propagates along z is hence described as follows:

$$\Phi(x,z) = \sum_{m=0}^{M-1} C_m \phi_m(x) e^{-j\beta_m z} \tag{2.18}$$

where the β_m's are the propagation constants of each mode and M the modes supported by the slab. For each mode m, the transverse wavevector is given by $k_{xm} = (m+1)\pi/W_e$, where W_e is an effective width which accounts for the lateral penetration of the evanescent mode into the cladding region and the polarisation dependence [8]. The longitudinal propagation constant is $\beta_m^2 = n_s^2 k_0^2 - k_{xm}^2$ where $k_0 = 2\pi/\lambda$ and n_s is the slab index. Using the binomial expansion with $k_{xm}^2 \ll k_0^2 n_s^2$, the propagation constants can be derived as:

$$\beta_m \approx n_s k_0 - \frac{(m+1)^2 \lambda \pi}{4 W_e^2 n_s} \tag{2.19}$$

Therefore, the propagation constants show a nearly quadratic dependence with respect to the mode number m. By defining L_π as the beat length between the fundamental and first order modes:

$$L_\pi = \frac{\pi}{\beta_0 - \beta_1} \approx \frac{4 n_s W_e^2}{3\lambda} \tag{2.20}$$

The propagation constants spacing can then be written as follows:

$$(\beta_0 - \beta_m) \approx \frac{m(m+2)\pi}{3L_\pi} \tag{2.21}$$

It can be derived from equations 2.21 and 2.18 that, when considering general interference [2], single replicas will occur at $L = 0,\ 2\times 3L_\pi,\ 4\times 3L_\pi,\ 6\times 3L_C,\ ... = p\times 3L_\pi$ for p even, i.e, that all guided modes will interfere with the same relative phases as in z=0. Single replicas will also occur at $L = 3\times 3L_\pi,\ 5\times 3L_\pi,\ 7\times 3L_C,\ ... = p\times 3L_\pi$ for p odd, however, in this case the replicas will be mirrored with respect to the plane $y = 0$, as described in Figure 2.16. Furthermore, at half-way distance between the direct and mirrored replicas, a pair of images

[1] The Overlap Integral is a quantitative measure of the overlap of atomic orbitals situated on different atoms.

[2] In general interference, the self-imaging mechanisms are independent of modal excitation

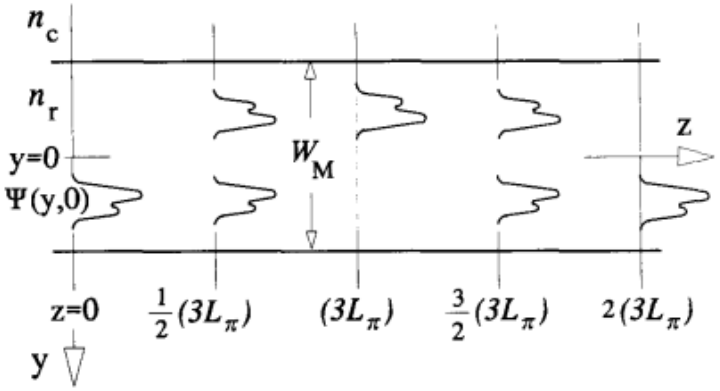

Figure 2.16: Input field $\Phi(y, 0)$ replicas in multimode waveguide [10]

will occur in quadrature and with amplitudes $1/\sqrt{2}$. This two-fold imaging is useful to realise 2x2 3-dB couplers. The detailed deduction of these results can found in [10].

2.3.6 Grating Couplers

A grating coupler is a periodic structure that can diffract light from propagation in the waveguide to free-space. It is normally used as an I/O device to couple light between fibre and sub-micrometer Silicon-on-insulator (SOI) waveguides. Figure 2.17 shows a schematic of a cross section of a grating coupler, where Λ is the grating period, W is the width of the

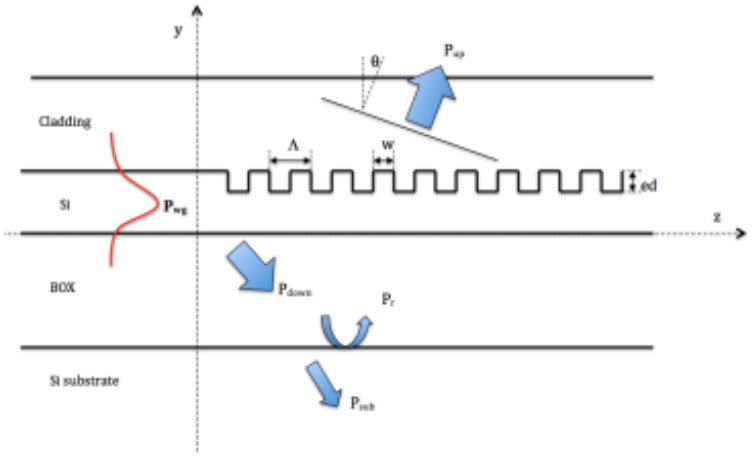

Figure 2.17: schematic of a cross section of a grating couple [11]

grading teeth (assuming uniform grating) and ed is the etch depth of the grating.
The behaviour of this component can be understood in terms of the Huygens-Fresnel principle, namely the constructive and destructive interference arising from the wavefronts created by the diffraction of light from the grating teeth. One dimensional grating couplers are well

described by the *Bragg Law*. The general form of the *Bragg condition* can be expressed as:

$$\beta - k_x = m \cdot K \tag{2.22}$$

where β is the propagation constant of the waveguide $\beta = \frac{2\pi n_{eff}}{\lambda_0}$ (where n_{eff} is the effective index of the slab waveguide), k_x is the wave vector of the diffracted wave in the direction of the incident wave, and K is the periodicity of the grating described as $K = 2\pi/\Lambda$. From the Bragg condition, it is possible to derive an expression for the grating period (see [11] for a detailed derivation):

$$\Lambda = \frac{\lambda}{n_{eff} - \sin(\theta_{air})} \tag{2.23}$$

where θ_{air} is the angle between surface normal and the propagation direction of the diffracted light, in the air.

2.4 Optical Ring Resonators

Since Optical Ring Resonators are the main component in the proposed implementation of an optical beamformer, an entire section of this chapter was dedicated to this topic, in order to present an overview of the fundamental properties and main applications of this device.

2.4.1 Fundamental properties of ring resonators

A generic *optical ring resonator* (ORR) consists of an optical waveguide which is looped back on itself, such that a resonance occurs when the optical path length of the resonator is exactly a whole number of wavelengths [24]. The term ring resonators can refer to any kind of looped resonator, not strictly circular rings. When the ring cavity is elongated, consisting of two 180° circular waveguides and two straight waveguides (along the coupling section) the term *racetrack resonator* is also used [4]. This device is only useful when coupled to the outside world, such that an optical signal can be fed into the ring cavity through a *bus waveguide*. The coupling mechanism typically consists of one or two *directional couplers*. Thus, there are two main types of ORR: All-pass and Add-Drop, as shown in Figure 2.18

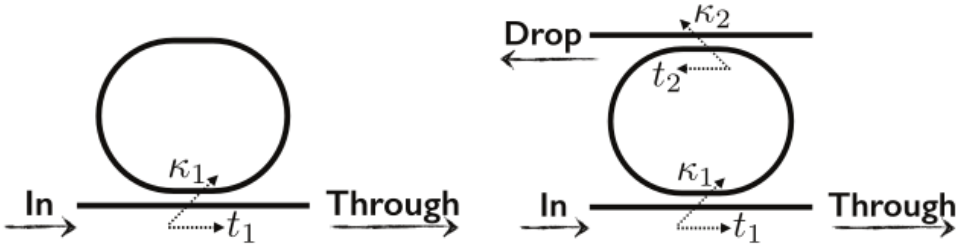

Figure 2.18: Diagram of racetrack resonators: All-pass (left) and Add-drop (right) [4]

2.4.1.1 All-Pass ring resonators

A simple ring resonator can be constructed by feeding the output of a directional coupler back into its input, known as an *all-pass* or *notch* configuration, Figure 2.18 (left). This leads to a two-port device, which acts as an all-pass filter and introduces a wavelength dependent phase shift [12]. Assuming the reflections back into the bus waveguide are negligible, the ratio of transmitted and incident field in the bus waveguide can be described as[3]:

$$\frac{E_{thru}}{E_{input}} = e^{i(\pi+\phi)}\frac{a - te^{-i\phi}}{1 - tae^{i\phi}} \tag{2.24}$$

Where t is the transmission coefficient through the coupler, or *self-coupling coefficient*; $\phi = \beta L$ is the round trip optical phase shift, with L the round trip length and β the propagation constant of the mode circulating in the waveguide. a is the single-pass amplitude transmission, which relates to the power attenuation coefficient α $[cm^{-1}]$ as $a^2 = e^{-\alpha L}$. The intensity transmission T_n (n as in notch) is obtained by squaring Eq. 2.24:

$$T_n = \frac{I_{thru}}{I_{input}} = \frac{a^2 - 2ta\cos\phi + t^2}{1 - 2at\cos\phi + (ta)^2} \tag{2.25}$$

It is also worth mentioning that resonance occurs when ϕ is equal to multiples of 2π, i.e, when the light wavelength fits a whole number of times inside the length of the loop, hence the resonance wavelength follows:

$$\lambda_{res} = \frac{n_{eff}L}{m}, \quad m = 1, 2, 3, ... \tag{2.26}$$

2.4.1.2 Coupling in ring resonators

As mentioned above, the linear waveguides are coupled into the ring waveguides via directional couplers. When the light beam crosses the linear waveguide, part of the light will be coupled into the ring due to the evanescent field outside the waveguide, which decays exponentially with distance [26]. Similarly to the transmission coefficient t, one can define a cross-over coupling coefficient k, so that t^2 and k^2 are the power splitting ratios of the coupler and for lossless coupling to occur, the following equation must be satisfied:

$$t^2 + k^2 = 1 \tag{2.27}$$

Another fundamental property of waveguides coupled to resonators is the condition of *critical coupling*. It refers to the condition in which internal resonator loss and waveguide coupling loss are equal for a matched resonator-waveguide system, at which point the resulting transmission at the output of the waveguide goes to zero on resonance [27].

[3]These properties were derived assuming light is operated in continuous wave CW mode, i.e, not pulsed [25]

2.4.1.3 Add-drop ring resonators

The *add-drop* ring resonator, Figure 2.18 (right), consists of a ring resonator that is coupled to two waveguides, resulting that the incident field is partly transmitted to the drop port. The transmission intensity equations for the drop and through ports are presented below [24].

$$T_{thru} = \frac{I_{thru}}{I_{input}} = \frac{t_2^2 a^2 - 2t_1 t_2 a \cos\phi + t_1^2}{1 - 2t_1 t_2 a \cos\phi + (t_1 t_2 a)^2} \tag{2.28}$$

$$T_{drop} = \frac{I_{drop}}{I_{input}} = \frac{(1 - t_1^2)(1 - t_2^2)a}{1 - 2t_1 t_2 a \cos\phi + (t_1 t_2 a)^2} \tag{2.29}$$

2.4.1.4 Spectral characteristics

As referred in section 2.4.1.1, when the effective wavelength of the optical signal is a multiple of the ring loop length, a resonance occurs and light interferes constructively and 'builds up' inside the ring. Hence, the ring response as a function of wavelength at the output ports will be periodic, with peaks at resonant wavelengths, as shown in Figure 2.19. In the through port, the ring exhibits a minimum at resonance. The difference in position between two consecutive resonant peaks, see Figure 2.19, is called Free Spectral Range (FSR) and can be defined either in frequency or wavelength domain: [12]

$$FSR_f = \frac{c}{n_g L}, \quad FSR_\lambda = \Delta\lambda \approx \frac{\lambda^2}{n_g L} \tag{2.30}$$

Where n_g is the wavelength group index and L is the round-trip length of the resonator. n_g is defined as: [8]

$$n_g = n_{eff}(f_o) + f_o \frac{dn_{eff}}{df}\bigg|_{\lambda_o} \tag{2.31}$$

With n_{eff} as the *effective refractive index* and f_o defined as $f_{1,2} = f_o \pm \Delta f/2$, with f_1 and f_2 as two consecutive resonant frequencies. From Equation 2.24, 2.28 and 2.29, the Full Width at Half Maximum (FWHM) of the resonance spectrum can be derived for all-pass and add-drop ring resonator configurations respectively:

$$FWHM = \frac{(1 - ra)\lambda_{res}^2}{\pi n_g L \sqrt{ra}} \tag{2.32}$$

$$FWHM = \frac{(1 - r_1 r_2 a)\lambda_{res}^2}{\pi n_g L \sqrt{r_1 r_2 a}} \tag{2.33}$$

It is also worth mentioning the quality factor (Q-factor) of an ORR, which is a measure for the sharpness of the resonance relative to its central frequency.

$$Q - factor = \frac{\lambda_{res}}{FWHM} \tag{2.34}$$

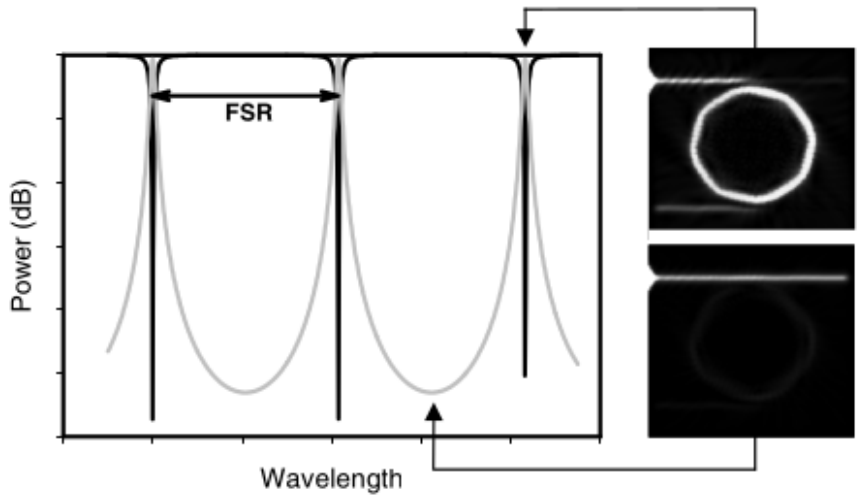

Figure 2.19: Simulated response of a Add-drop ring resonator for the through- (black) and drop port (grey). Also shown is the Free Spectral Range, the distance between two consecutive fringes. At the right simulated fields of the MR are given; top: ON resonance, Bottom: OFF resonance [12]

2.4.1.5 Sensitivity

ORR resonance is dependent on the round trip length of the ring as well as in the losses (both in the coupler and due to waveguide propagation). Hence, this makes ring resonators highly sensitive to numerous effects. The high sensitivity of ORR is an attractive feature for sensing applications and it is generally quantified by the amount of wavelength shift $\Delta\lambda_{res}$ caused by a certain varying amount or effect one is interested in studying, be it temperature, physical deformation or changes in the waveguide composition. From eq. 2.26 it is easy to conclude that a shift in wavelength essentially is a result of a shift in the effective index of the resonant mode [24]:

$$\Delta\lambda_{res} = \frac{\Delta n_{eff} L}{m}, \quad m = 1, 2, 3, ... \tag{2.35}$$

2.4.2 Resonance wavelength tuning

So far ring resonators have been assumed to be totally passive, i.e it has been assumed that all geometrical and material parameters are constant in time. However, either to add functionality or to overcome fabrication errors, it may be necessary to vary some of the parameters and the resulting wavelength response [12].
The most widely form of tuning used is thermal tuning, by applying heat to the ring, resulting in a variation of the ring refractive index. This is especially the case in silicon based circuits, due to the large thermo-optic response of silicon [24] [4].
Other tuning methods include Electro-optic effect: where an electrical field is applied to cause change in the refractive index; Carrier injection: optical pumping that creates free carriers

(single photon or two-photon absorption), which changes the loss parameter and the refractive index of the material; or even Opto-optical effect: where light itself causes change in index via nonlinear effects [12].

2.4.3 Applications of ring resonators

Ring resonators, albeit a simple concept, are useful in numerous applications. Due to its frequency selective behaviour, described in previous sections, ring resonators can be used as optical filters. These are quite useful in communication applications, such as Wavelength Division Multiplex systems to multiplex and demultiplex signals.
As mentioned in section 2.4.1.5, due to its sensitivity, ORR ideal components for a variety of sensing applications, such as temperature sensing, chemical, biological or medical: for example in drug compound analysis or antibodies detection in fluids [24].
ORR can also be actively tuned, see 2.4.2, to be used as electrically actuated devices, like modulators [4].

2.4.3.1 Optical Delay Lines

Near resonance, ORR will have a strong dispersion and, therefore, a large group delay will be introduced. Thus, these devices can be used as *optical delay lines*. This application constitutes the basis of the optical beamforming design approach proposed in this project and is explored in further detail in the following chapter 3.
Optical delay lines are commonly made up of all-pass filters ring resonators. All-pass ORR have a large group delay at resonance and a unity magnitude of response (when the losses in the waveguide and ring are negligible). Figure 2.20 shows a theoretical group delay of an all-pass ring delay based element. The group delay of a single all-pass ORR can be obtained by differentiating the phase response of the filter with respect to frequency. Just like the phase response, the group delay response will be periodic with the same FSR:

$$\tau_{gi}(f) = \frac{k\tau_r}{2 - k - 2\sqrt{1-k}\cos 2\pi f\tau_r + \phi} \tag{2.36}$$

Where τ_r is the round-trip time, which is equal to the inverse of FSR and k is the cross-over coupling coefficient, and ϕ is the round-trip phase shift of the ring. In order to increase the bandwidth of the group delay, several ORRs can be cascaded, as illustrated by Figure 2.21 . It can be shown that the total group delay τ_g can be found by summing the individual group delays τ_{gi} (assuming a lossless waveguide) and is given by:

$$\tau_g(f) = \sum_{i=1}^{3} \frac{d\Phi_i(f)}{df} = \sum_{i=1}^{3} \frac{k\tau_r}{2 - k - 2\sqrt{1-k}\cos 2\pi f\tau_r + \phi} \tag{2.37}$$

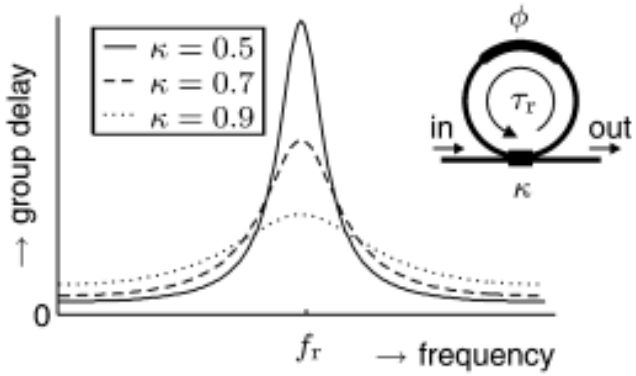

Figure 2.20: Ring resonator group delay, for different values of cross-over coupling coefficient [13]

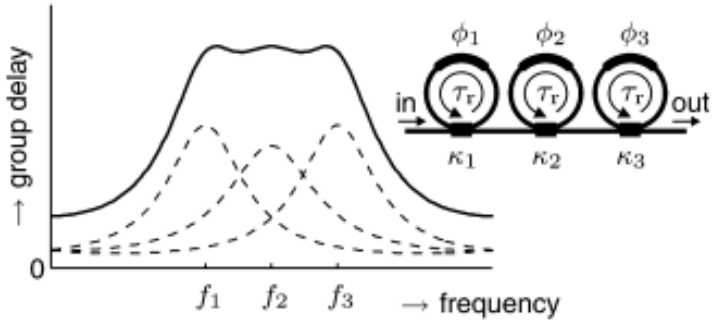

Figure 2.21: Ring resonator group delay response of three cascaded ORR [13]

An example of an optical delay line is presented in [14]. It is composed of three All-pass ORR cascaded and connected to the waveguide by variable couplers. Heaters are located on the ring for tuning the resonance frequency, and on one of the branches of the channels of the MZI ring coupler for adjusting the power coupling to the ring. The delay can thus be tuned by varying the amount of power coupled to the ring. The ORRs used by this article have a radius of 3.12 mm, but nowadays silicon ORR can be manufactured with radius rounding the tens of micrometers and integrated in an photonic circuit. Figure 2.22 contains a diagram of the optical delay line structure.

2.5 PIC Beamformer Implementations

Although Optical Beamforming has been around since the 1990s [18], this area has only reached fruition quite recently. Optical architectures are often associated with True-Time-Delay. Among others, these solutions include active element switching [28], Optical Delay Line switching or Bragg-grating based delay lines [29]. Furthermore, there are solutions for multi

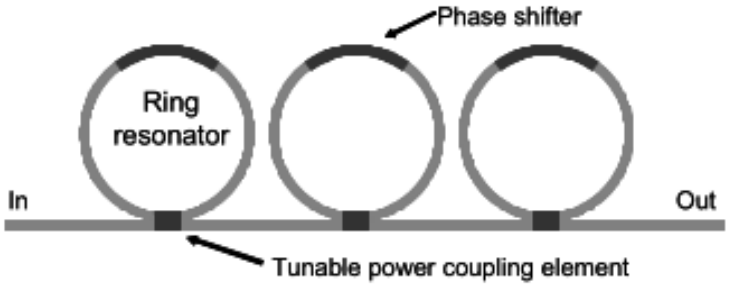

Figure 2.22: Diagram of the 3-stage ring resonator filter [14]

beam optical beamforming, such as the one proposed by [30], that is based on Wavelength Division Multiplex and Dispersion Fibre.
Implementations for optical bemformers based on tunable delay lines [13] [14] present an interesting solution with lower switching times compared to other implementations where, for example, the optical signal is switched between different optical paths. On the other hand, the range of frequencies affected by flat delay generated by this implementation increases with the increase in complexity of the circuit, namely, the number of ORR in the system. An alternative proposed by [31] eliminates this dependence by separating the optical carrier from the sidebands and applying a phase shift to the carrier, which requires a lower delay bandwidth.
As mentioned in section 1.3, this project proposes a design approach for a tunable delay unit based on ORR.

2.6 Summary

In the present chapter, an overview of the State-of-the-art was provided. The relevant topics concerning this project, from Phased Array Antennas, basic optical components to PIC beamformer implementations were reviewed and a theoretical analysis was provided. Optical Ring Resonators were given particular attention in this chapter, since they constitute the most important aspect for the beamformer design.

Chapter 3

Delay Unit Design

3.1 Introduction

The present chapter contains a detailed design description of the Delay Unit. This device is responsible for inducing a fully controllable broadband time delay to an input optical signal. The Delay Unit constitutes, therefore, the most fundamental component in the optical beamformer architecture.
This chapter begins with a section containing the delay unit definition and its main specifications. Subsequently, some fundamental ring resonator characteristics are described, supported by analytical and simulation results. This is followed by three sections dedicated to each functional requirement for the proposed device, where the design decisions made in order to meet said requirements are presented, as well as the results that justify them. The chapter concludes with an overview of the device's final architecture and a summary.

3.2 Device Specifications

Firstly, it is important to define the term *Delay Unit*. A Delay Unit should constitute a device that takes a signal as input and is capable of applying a time delay to that signal. Such time delay or phase shift should be tunable, i.e, the amount of delay applied to the input signal should be controllable. Moreover, the applied delay should be constant over the whole frequency range of the input signal, or, at least, its variation should be minimised as much as possible. This aspect is crucial, in order to avoid *beamsquint* [16].
A list of specifications that the system must comply with is presented below:

- The delay unit must be tuned for a phased array antenna working in the Ka Band, namely at $29.5\,\text{GHz} - 30\,\text{GHz}$ frequency range. This implies that the device must provide a flat time delay over the $500\,\text{MHz}$ signal bandwidth. As referred in chapter 1, this beamformer is intended for satellite communications, thus the phased array signal frequency band was chosen taking into account recent technologies of broadband satellite communications, such as those referred in [32][19][33].

- The device must enable a tunable delay range that corresponds to a phase shift from 0° to 360°. The phase span is determined based on the beam scanning range required and the antenna array geometry intended for the application. These aspects are explained in greater detail in chapter 5.

- The delay unit must enable a minimum delay step that provides a phase shift resolution of 1°.

- The device must be realised in silicon photonic technology, thus allowing integration on a photonic chip. The circuit must operate at the C-band (namely a 1550 nm optical wavelength).

3.3 Ring Resonator Spectral Characteristics

Ring resonators have interesting properties, namely that they can be used to introduce time delays, as optical delay lines, as described in 2.4. In this section, a set of ORRs are simulated, using the PIC simulation software *Interconnect* (which is part of *Lumerical* simulation package), in order to obtain a delay line suitable for the project's application. The simulation software Interconnect performs circuit level simulations of photonic components [34], which is of great interest when defining the circuit's overall architecture.

3.3.1 Transmission and Free Spectral Range

Firstly, a single all-pass ORR with 30 µm radius was simulated in Interconnect, using components from the software library. The ring was divided into segments and the schematic is depicted in Figure 3.1. The ORR is comprised of a straight waveguide and a 2x2 waveguide directional coupler to perform the input/output coupling. The coupler is connected to an ONA, or *Optical Network Analyser*, which performs scattering analysis to calculate the overall circuit performance. The waveguide has a length of $2\pi \times 30\,\mu m = 188.495\,\mu m$, which corresponds to the full length of a circular ring, because the coupler length can be ignored [1]. The coupler is set to a default coupling coefficient of 0.3. It should be noted that, although a straight waveguide is being used to simulate a circular ring, this schematic is equivalent to using a circular waveguide, since the simulation software takes care of the connections to the coupler, as mentioned in [35].
From [24] [12], it is known that the transmission response has a frequency dependent response, that is periodic and described by the following expression:

$$T_n = \frac{I_{thru}}{I_{input}} = \frac{a^2 - 2ta\cos\phi + t^2}{1 - 2at\cos\phi + (ta)^2} \tag{3.1}$$

[1] This is true for the ideal library component, which has "0 m" length. This is not the case for the directional coupler used from the PDK. See 3.4.1.

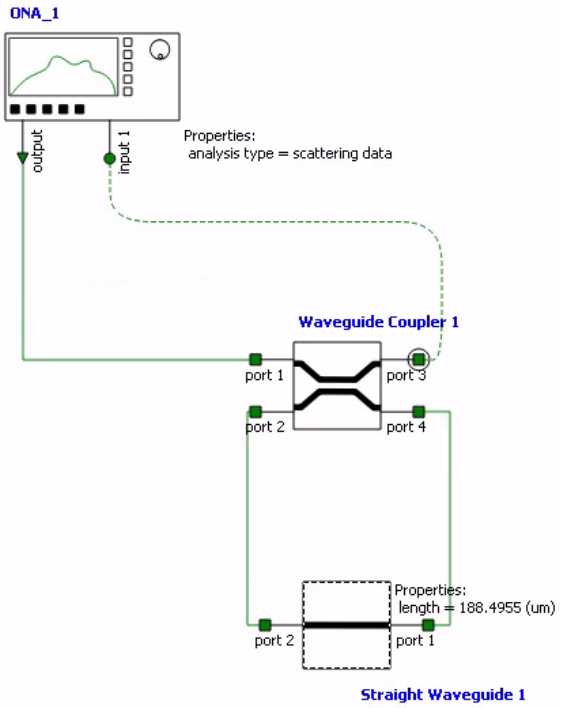

Figure 3.1: Single All-pass ORR schematic

where t is the transmission coefficient through the coupler, or *self-coupling coefficient*; $\phi = \beta L$ is the round trip optical phase shift, with L the round trip length and β the propagation constant of the mode circulating in the waveguide. a is the single-pass amplitude transmission, which relates to the power attenuation coefficient α $[cm^{-1}]$ as $a^2 = e^{-\alpha L}$.
The transmission response of this schematic has a magnitude of 1 for the whole ONA frequency sweep range. This can explained by the configuration of an all-pass ring (see 2.4.1.1), which guides all the incident light back to the bus waveguide (in this case, the ONA), acting as an all-pass filter, and by the fact that both the coupler and the waveguide are ideal lossless components, thus the attenuation coefficient of this circuit is $\alpha = 0$ and the single-pass amplitude transmission is equal to $a = e^{0L} = 1$. Figure 3.5 depicts the transmission response for the ideal case where $a = 1$ and a non-ideal schematic, where there are inherent losses and $a < 1$. It should also be noted that all possible reflections were assumed negligible. This aspect is dealt with in the layout design, with the integration of adiabatic bends, see 5.4.1. The transmission phase response and a plot of the transmission response in the real domain are depicted in Figures 3.2 and 3.3. To better understand the all-pass ring phase response, one can derive from 2.24 the effective phase shift Φ induced by the all-pass ring:

$$\Phi = \pi + \phi + \arctan\frac{r\sin\phi}{a - r\cos\phi} + \arctan\frac{ra\sin\phi}{1 - ra\cos\phi} \tag{3.2}$$

As expected from equation 3.2, the results in Figure 3.2 show π phase shifts occurring

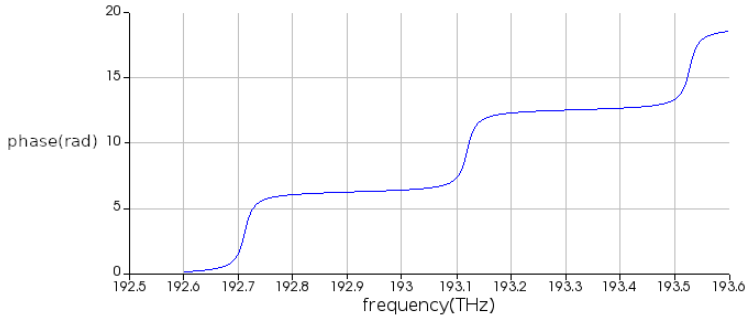

Figure 3.2: Transmission Phase

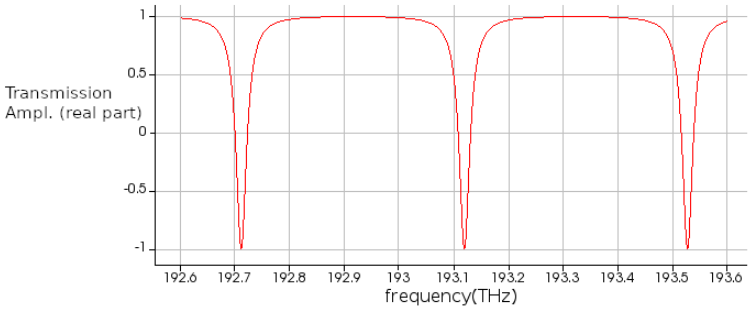

Figure 3.3: Transmission response plot (Real part)

periodically at every resonant frequency, i.e, when the light wavelength is equal to $\lambda = \frac{n_{eff}L}{m}$ with $m = 1, 2, 3, ...$ From theses results, it is possible to measure the *Free Spectral Range*, by taking the difference in frequency between two notches in the real part of the transmission response or between two phase shifts in the phase response plot, which results in a $FSR = 408\,\text{GHz}$. This value can validated by calculating the FSR using the analytical expression, and the waveguide group index imposed by the simulation software $n_g = 3.9$:

$$FSR_f = \frac{c}{n_g L} = \frac{299792458}{3,9 \times 2\pi \times 30 \times 10^{-6}} = 407.8\,\text{GHz} \tag{3.3}$$

Once the *Process Design Kit*, or PDK, was made available by the foundry *IMEC*, the ideal components were replaced by the PDK corresponding components. The previous simulations were replicated with the PDK components (see Figures 3.4 and 3.5). Note that in this case the length of the waveguide coupler can not be neglected and must be subtracted from the ring length, which was set to 183.1455 µm. Moreover, the FSR is not identical to the former circuit ($FSR = 347\,\text{GHz}$), since the PDK waveguide group index is different (approximately 4.58). In addition, the transmission magnitude is not unity for all frequencies, as illustrated in Figure 3.5. This is due to the losses inherent to the PDK coupler and waveguide. As expressed in equation 3.3, the FSR is inversely proportional to the round trip length of the ring, and can be a determining factor for some ring designs, especially ring-based optical filters [12]. However, in this project, the FSR was not so relevant for the design, compared to other

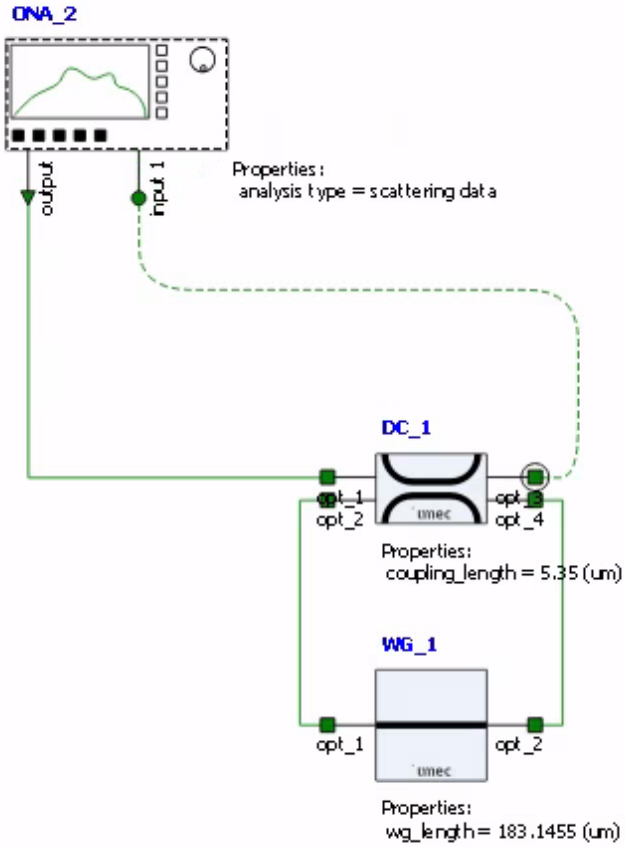

Figure 3.4: All-pass ORR with PDK components

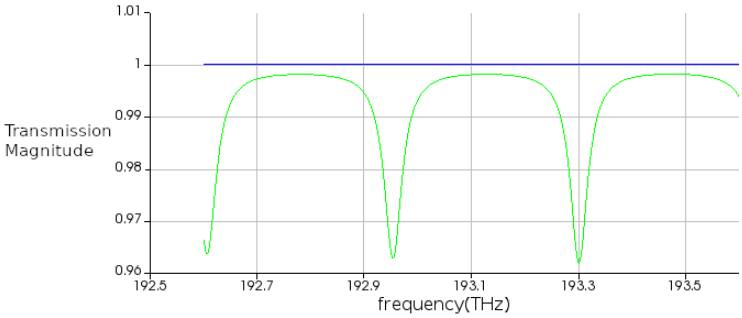

Figure 3.5: Transmission magnitude response (blue: ideal components/ green: PDK components)

more important factors discussed in the subsequent sections, which have conditioned the ring dimensions.

3.3.2 Group Delay Response

As explained in detail in section 2.4.3, the group delay response of an ORR, will be a periodic function, with FSR as the period, according to the following expression [13]:

$$\tau_{gi}(f) = \frac{k\tau_r}{2 - k - 2\sqrt{1-k}\cos 2\pi f\tau_r + \phi} \tag{3.4}$$

Where τ_r is the round-trip time, which is equal to the inverse of FSR and k is the cross-over coupling coefficient, and ϕ is the round-trip phase shift of the ring. Therefore, the group delay response is dependent on the ring dimensions, the coupling coefficient of the bus-to-ring coupler and the phase shift induced by the ring.
Considering the PDK schematic referred in the previous section (Figure 3.4), the group delay response of a single All-pass ORR is depicted in Figure 3.6.

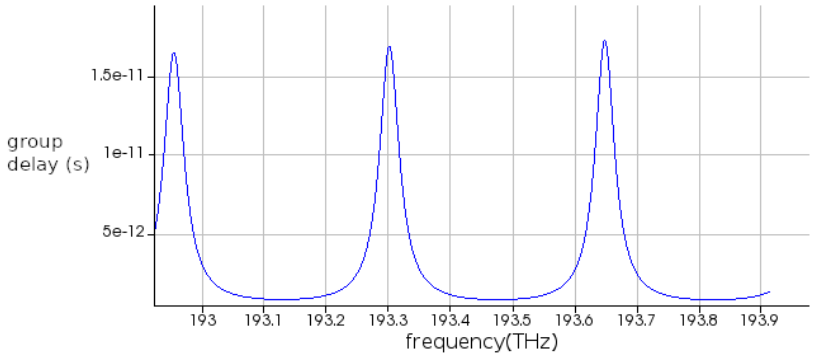

Figure 3.6: All-pass ORR group delay response

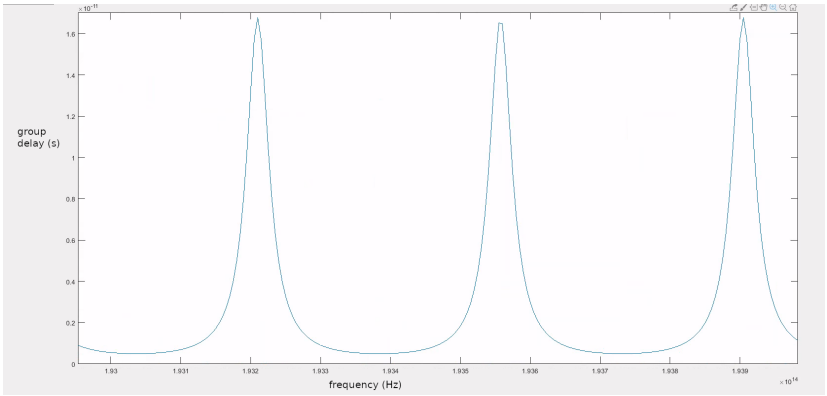

Figure 3.7: Theoretical delay model plot

The simulation results are consistent with the analytic delay equation, with an FSR equal to 347 GHz and a peak amplitude of 16.961 ps. Figure 3.7 depicts a plot of equation 3.4 as a function of frequency, using MATLAB. It can be observed that the FSR and delay amplitude

are almost identical, except for a shift in frequency, because ϕ was set to 0 in the theoretical model.

In order to observe the group delay response as a function of the coupling coefficient, the circuit was simulated for 3 values of the coupling coefficient (0.5;0.7;0.9). The same was done for the theoretical model, so as to validate the simulation results. Figures 3.8 and 3.9 show the ring simulation group delay response and the theoretical model, respectively. The results demonstrate that the group delay amplitude decreases with the increase of the coupling coefficient. Therefore, by changing the coupling coefficient, one can control the amplitude of the group delay induced by the ORR. This will be expanded in section 3.4.

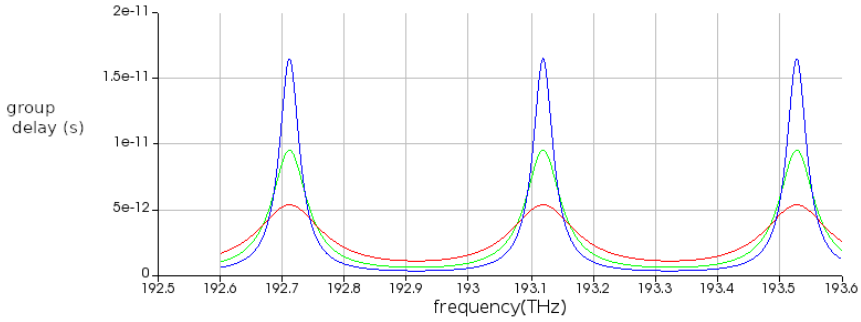

Figure 3.8: ORR Group delay response as a function of coupling coefficient (blue: 0.5; green: 0.7; red: 0.9)

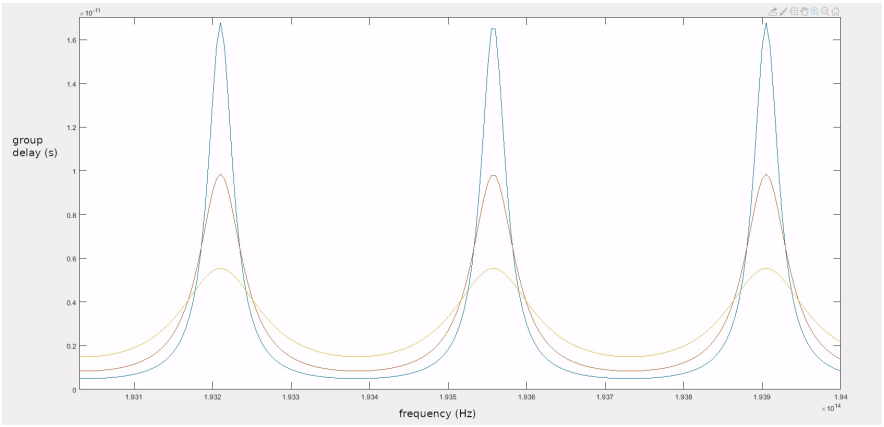

Figure 3.9: Theoretical model as a function of coupling coefficient (blue: 0.5; orange: 0.7; yellow: 0.9)

For the purpose of observing the group delay response as a function of the ring round-trip phase shift, a thermo-optic phase shifter was added to the ring loop, as illustrated in Figure 3.10. The circuit was simulated for different phase shift values, namely $0, \frac{\pi}{4}, \frac{\pi}{2}, \frac{3\pi}{4}$ and the results are presented in Figure 3.11 As expected from the analytical model 3.4 (see also model

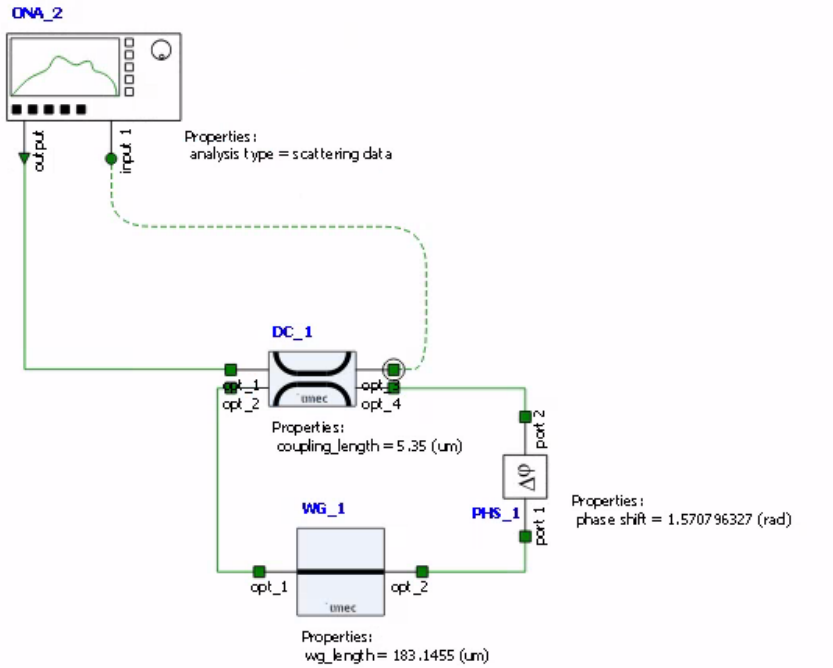

Figure 3.10: All-pass ORR with phase shifter

plot in Figure 3.12) the resonant frequency, i.e, the frequency where the delay peak occurs, decreases when the ring round trip phase shift (ϕ) is increased.

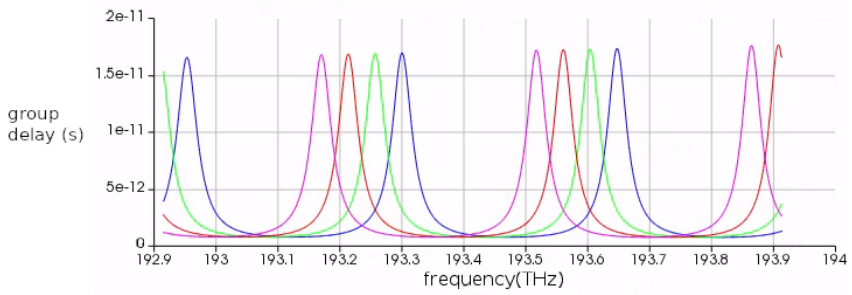

Figure 3.11: ORR Group delay as a function of round trip phase (blue: 0; green: $\frac{\pi}{4}$; red: $\frac{\pi}{2}$; purple: $\frac{3\pi}{4}$)

Two more 30 µm radius rings were added in series, in order to simulate and verify if it is possible to obtain a wider group delay bandwidth [13][31]. The resulting schematic is described in Figure 3.13, and contains three rings cascaded, each with an incremental round-trip phase, tuned with a phase shifter, as shown in table 3.1: The simulation results are depicted in Figure 3.14, and it can be concluded that the resulting group delay response of a series of cascaded rings is equivalent to the sum of the individual ring delay responses, as expected from 2.37. Moreover, by cascading rings it is possible to apply a group delay over a wider range

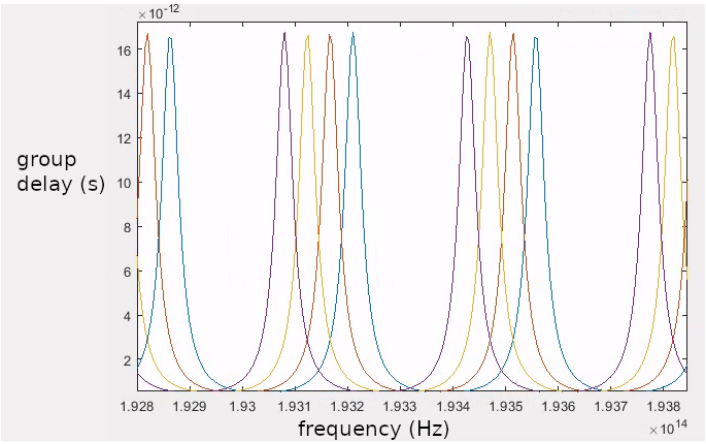

Figure 3.12: Theoretical model of the group delay as a function of round trip phase (blue: 0; orange: $\frac{\pi}{4}$; yellow: $\frac{\pi}{2}$; purple: $\frac{3\pi}{4}$)

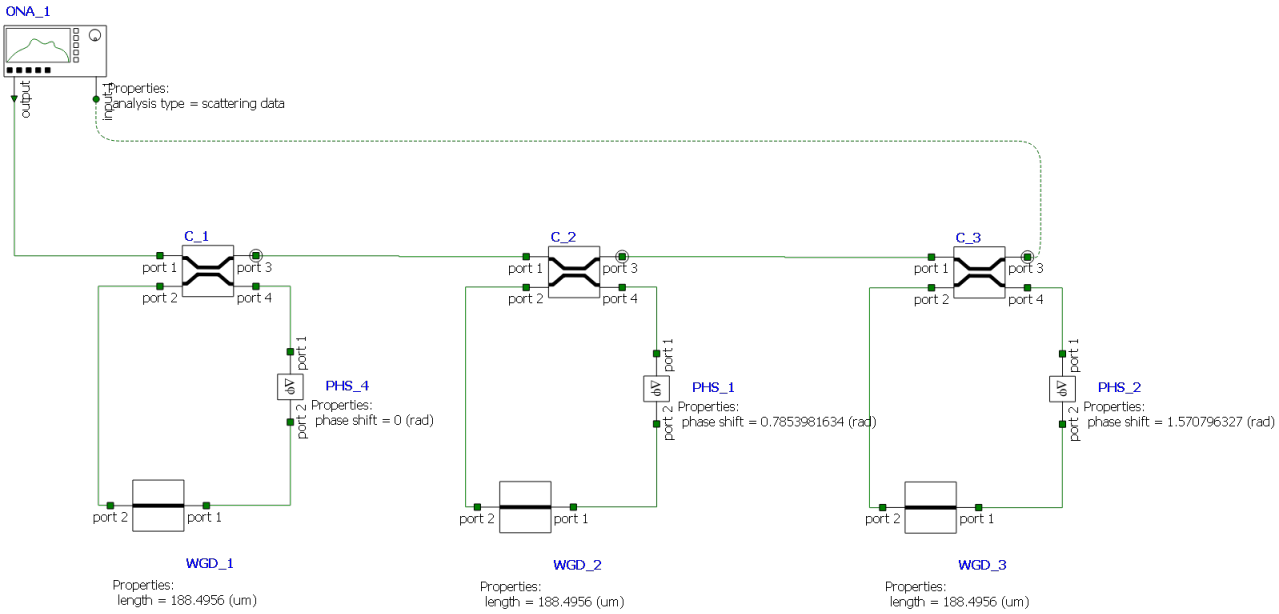

Figure 3.13: 3 cascaded ORR, with incremental round-trip phases

Ring	phase shift (radians)
1	0
2	$\frac{\pi}{4}$
3	$\frac{\pi}{2}$

Table 3.1: Round-trip phase shifts of cascaded rings

of frequencies. Considering a group delay amplitude of 16 ps, it is demonstrated in Figure 3.14 that the bandwidth is approximately 109 GHz, with a total variation, or ripple, of 5.2 ps.

Although the ripple is quite large relative to the total delay (which, in turn, deteriorates the beam scanning resolution), the delay bandwidth is considerably larger than for a single ORR, which is approximately 12 GHz, for the same delay amplitude and a maximum ripple of 1.736 ps. Both the maximum acceptable ripple and delay bandwidth are important constraints for a delay line. These aspects are explored in greater detail in sections 3.4.2 and 3.5.2, respectively.

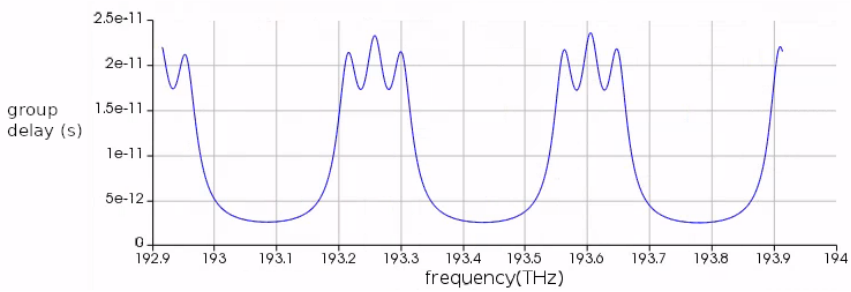

Figure 3.14: 3 cascaded ORR group delay response

3.4 Group Delay Amplitude Control

In the previous section, it was stated that the group delay response of an ORR is determined by three factors: the ring dimensions, the bus-to-ring coupling coefficient and the round-trip phase shift. If it is required to tune the delay amplitude in real-time, naturally, the first option is not feasible, since the ring dimensions will not be altered once the chip is fabricated. From 3.3.2, it was shown that the group delay amplitude is directly affected by the magnitude of the coupling coefficient. Therefore, it follows that in order to tune the group delay amplitude, it is necessary to somehow tune the cross-over coupling coefficient, i.e., how much optical power is coupled from the bus waveguide to the ring. This problem will be discussed in the present section as well as a possible solution for this problem.

3.4.1 Variable Coupler

3.4.1.1 Variable Coupler Model

Since a directional coupler was used to couple light in and out of the ring for the previous simulations, let us first exam the behaviour of this device. Directional coupling is defined as the power transfer between two neighbouring waveguides. As explained in sections 2.3.3 and 2.4.1.2, conventional directional couplers, consist of two parallel waveguides, which are placed close to each other, so that light is coupled from one waveguide to the other via the evanescent field outside the waveguide. Figure 3.15 shows a GDS file of a directional coupler designed for this project. The cross-over coupling coefficient, k, which describes the fraction

of power coupled from one waveguide to the other, can be expressed as [4]:

$$k^2 = \frac{P_{cross}}{P_0} = \sin^2(CL) \tag{3.5}$$

Where P_0 is the input optical power, P_{cross} is the power coupled across the coupler into the other waveguide, L is the length of the coupler and C is the coupling strength. The coupling strength is controlled by both the length of the coupler and the spacing between the two waveguides, often referred as *gap*. Once again, the same problem mentioned at the beginning of this section arises, because, the only apparent way to control the cross-over coupling coefficient is by changing the physical dimensions of the circuit, namely the dimensions of the coupling coefficient. A solution proposed by [15][20] is the implementation of a variable coupler, that

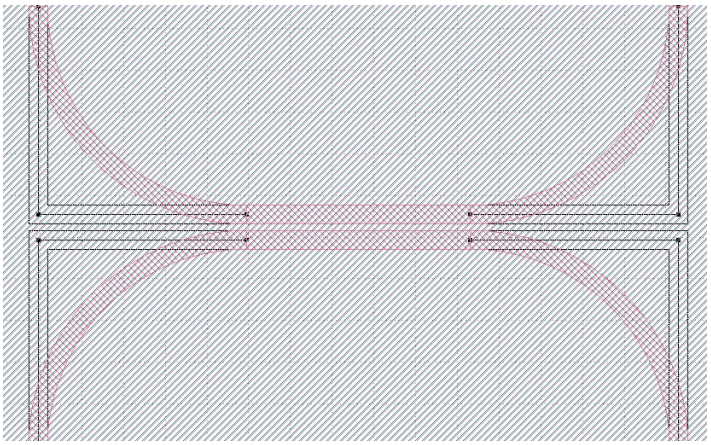

Figure 3.15: GDS layout of directional coupler developed for this project

enables one to control the cross-over coupling coefficient, via thermal tuning. The variable coupler consists of a *Mach-Zender Interferometer* (MZI) with phase shifters in one or both arms, as depicted in Figure 3.16. Connected at the input and output of the MZI structure are 2×2 3 dB directional couplers, i.e., approximately half of the power is coupled through to the other waveguide. The solution implemented in the project is based on the "type A" model proposed by [20], which consists of an MZI with equal length arms and a phase shifter in the upper arm, connected by 2×2 3 dB couplers, making it a 4-port device. By supplying an electric current to heat the waveguide, a desired phase shift is induced, which, in turn, controls the fraction of cross-coupled power. The device has two main working modes: it can work as a cross/bar switch, i.e., where all the power is coupled from *In1* to *Out2* [2], referred to as cross mode, and when none of the power is cross coupled, so that all the power is carried from *In1* to *Out1*, referred to as bar mode, see Figure 3.16; or it can work as a tunable power divider. This component can be modelled by a transfer matrix, with parameters $c_{ij} = Out_i/In_j$ and

[2] and vice versa, from *In2* to *Out1*.

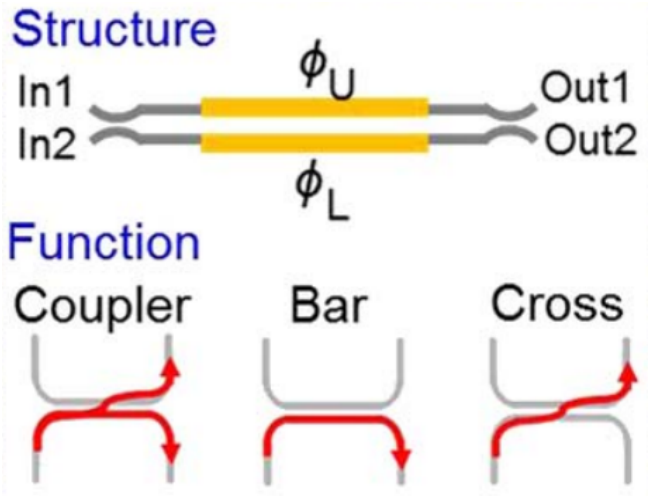

Figure 3.16: Variable coupler diagram and working modes [15]

the following expressions, according to [15]:

$$c_{11} = -c_{22} = -j\exp(j\phi_A)\cdot\sin(\phi_D)\exp(j2\pi\Delta_\tau) \quad \text{(bar port)} \tag{3.6}$$

$$c_{12} = -c_{21} = -j\exp(j\phi_A)\cdot\cos(\phi_D)\exp(j2\pi\Delta_\tau) \quad \text{(cross port)} \tag{3.7}$$

Where $\phi_A = (\phi_U + \phi_L)/2$ and $\phi_D = (\phi_U - \phi_L)/2$ [3], govern the phase and cross-coupling coefficient of its output ports, respectively. Thus, by controlling ϕ_D, the component will function as a tunable coupler when $\sin(\phi_D) > 0$ and $\cos(\phi_D) < 1$; a switch in bar mode when $\sin(\phi_D) = 1$ and $\cos(\phi_D) = 0$ or in cross mode when $\sin(\phi_D) = 0$ and $\cos(\phi_D) = 1$. The term $\exp(j2\pi\Delta_\tau)$ represents the phase shift caused by the propagation delay Δ_τ of the coupler.

3.4.1.2 Variable Coupler Implementation and Validation

For the circuit implementation of the variable coupler, the first step was to design the 3 dB directional couplers. There are two main design constraints in a directional coupler: the waveguide gap g and the coupling length L. The *IMEC* foundry's PDK directional coupler has a fixed gap equal to $g = 150$ nm. Thus, only the coupling length L has to be defined. In order to obtain the appropriate L for a -3 dB cross-over coupling ratio, a sweep of cross-over coupling gain as a function of the coupling length was conducted, with the results depicted in Figure 3.17. From these results, the coupling length was set to 5.35 µm and the cross-over coupling power gain (from the ONA *output* to *input 2*, in the schematic of Figure 3.19) was measured, so as to verify if the coupling length defined was yielding the expected cross-over coupling coefficient. As illustrated in Figure 3.18, the cross-over coupling coefficient is -3 dB,

[3] for the implemented component ϕ_L is constant, as there is no phase shifter.

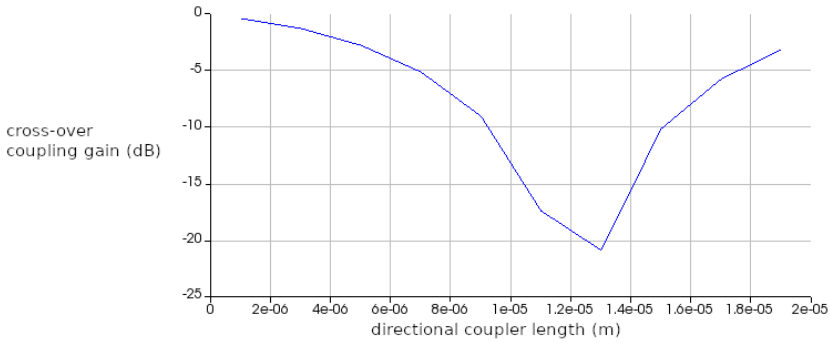

Figure 3.17: cross-over coupling power gain as function of coupling length

for the operational optical wavelength of 1550 nm, thus validating the chosen coupling length.

For the MZI implementation, the main control factor considered was the thermo-optic phase

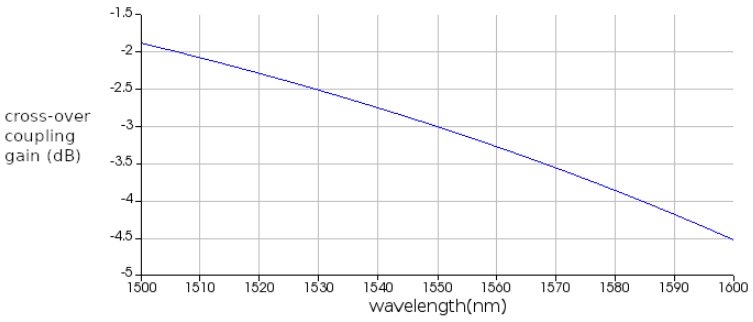

Figure 3.18: cross-over coupling power gain for $L = 5.35\,\mu m$ and operation wavelength $\lambda = 1550\,nm$

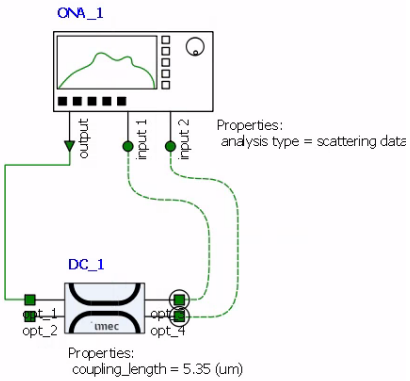

Figure 3.19: PDK Directional Coupler analysis schematic

shifter length. The thermo-optic phase shifters supplied by the *IMEC* PDK are made of strip waveguides with sections of n-type doped silicon on each side. They are available in chainable sections of 100 µm. The phase shifter length was set to the minimum length of 100 µm, in order to minimise the chip area and because longer lengths yielded no improvements, in terms of phase shift range. It should be noted that the phase shifter has two heater sections on each side of the waveguide, and each heater contains two electrical contacts, for the bias voltages that control the phase shift induced by the waveguide, as described in Figure 3.20. The phase shifter accepts bias voltages from 0 to 30 V. With all sub-components set, the variable coupler was assembled in the schematic depicted in Figure 3.21 and simulated. As a means to validate the functionality of the variable coupler, a sweep of the cross-over coupling power gain was conducted as a function of the phase shifter bias voltage. The results are given in Figure 3.22. It can be observed that the designed variable coupler has a maximum cross-over coupling gain excursion of 28.42 dB, with a power gain on the cross port of approximately 0 dB in cross mode and −28.42 dB in bar mode. This means that in cross mode, almost all

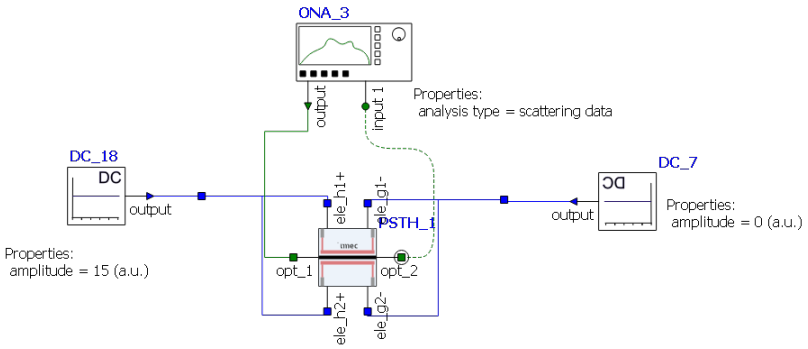

Figure 3.20: Phase shifter Interconnect block

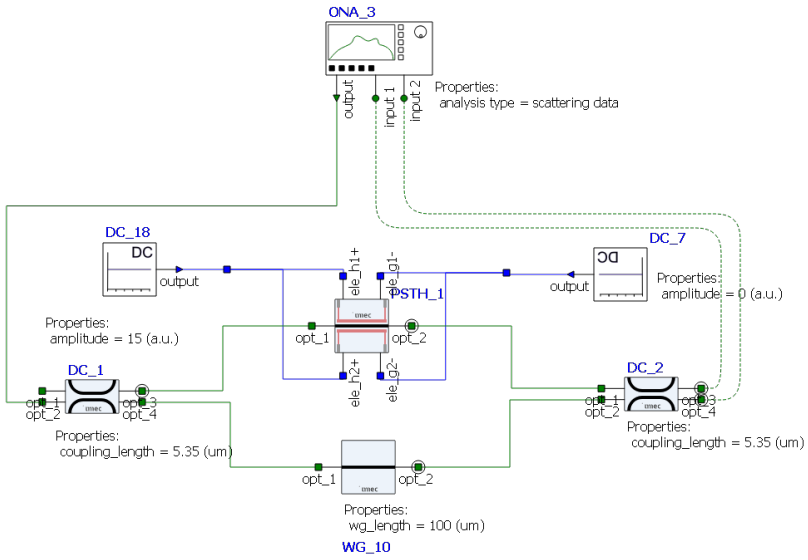

Figure 3.21: Variable Coupler schematic

the incoming optical power is coupled through the cross-port (cross-over coupling coefficient ≈ 1) and the coupled power can be progressively reduced to almost 700 times less in bar mode (cross-over coupling coefficient ≈ 0.001439). Furthermore, it is relevant to note that not the entire bias voltage range is of use for controlling the cross-over coupling coefficient. The usable bias voltage range is shown to be from 15 to 25 V.

3.4.2 Amplitude Range and Resolution

The previous sub-section 3.4.1 describes the analysis and design of a variable coupler that is capable of tuning the cross-over coupling coefficient magnitude from 1 to 0.001439. This component was designed, in order to enable a tuning of the group delay amplitude, which is necessary for inducing varying phase delays in the RF signals that, in turn, enables scanning the direction of maximum radiation in an antenna array.

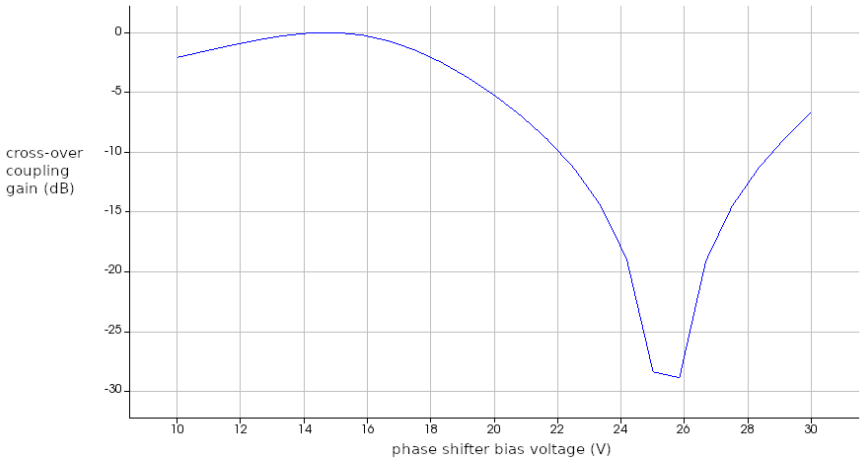

Figure 3.22: cross-over coupling power gain as a function of phase shifter bias

The variable coupler was connected to a 30 µm radius ORR, as a way of coupling the light from the bus waveguide into the ring and vice versa. The resulting schematic was connected to an ONA and is described in Figure 3.23. It should be noted that the length of the loop waveguide (WG_5) is equal to the round-trip length minus the MZI waveguide length and 2× the coupling length (for each directional coupler) $L = 1\,88.1455 - 100 - 2 \cdot 5.35 = 77.4455\,\mu m$. This group delay response of this circuit was simulated for a set of bias voltages of the variable coupler and the results are shown in Table 3.2 and plotted in Figure 3.24.

Bias Voltage (V)	group delay (ps)
15	6.47
17	9.01
18	11.08
20	19.01
21	27.22
22	43.56
22.5	58.04
23	81.84
23.5	120.71
24	194.64

Table 3.2: ORR + Variable Coupler Group Delay response (peak group delay as a function of Bias Voltage)

The results in 3.2 demonstrate that the circuit is working as expected, as it is capable of modulating the amplitude group delay. The variation of the full usable bias voltage range results in a group delay amplitude tuning from 6.47 ps to 194.64 ps and, therefore, a maximum amplitude range of $\Delta_{g\_delay} = 194,64 - 647 = 188.17\,ps$. Considering that for an RF signal centred at 29.75 GHz, a 2π phase shift corresponds to a time delay equal to a period, or $T = 1/f = 1/29.75\,GHz = 33.613\,ps$, this circuit is capable of introducing a maximum phase

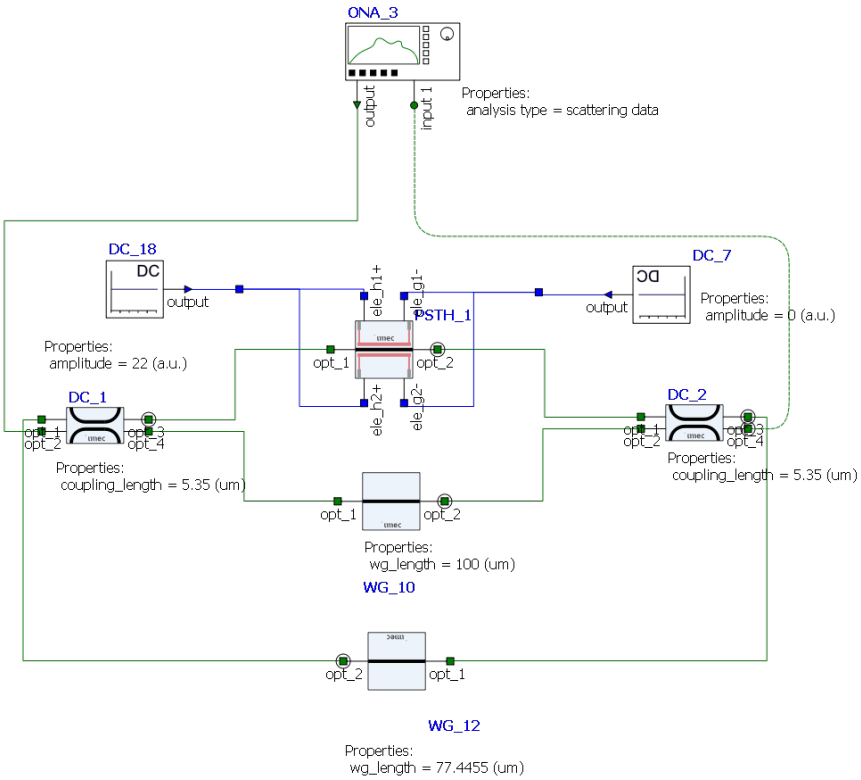

Figure 3.23: ORR connected to Variable Coupler

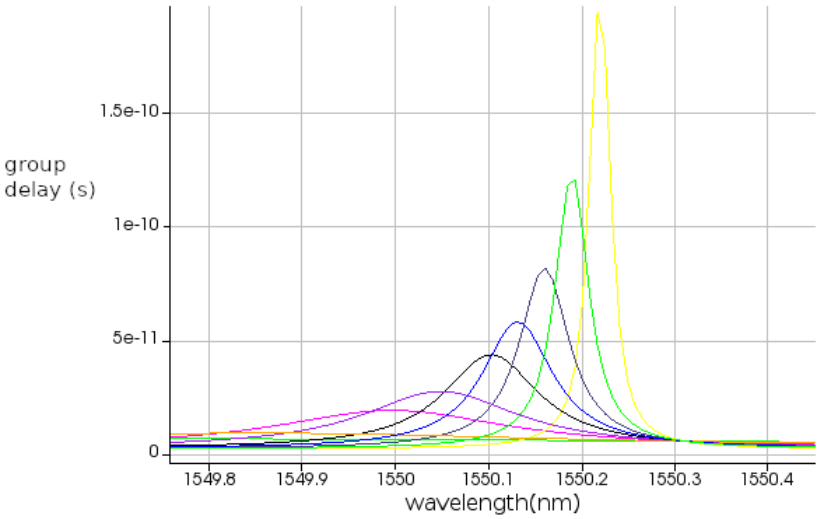

Figure 3.24: Group Delay Response Plot

delay larger than 10π, which greatly surpasses the requirement regarding range. However, as it is shown in 3.24, the peak width is more or less inversely proportional to the peak value, which can be a problem if the flat delay bandwidth is lower than the requirement. This is because the area underneath the group delay curve is constant and equal to 1 [13].

As stated in section 3.2, the delay unit should provide a minimum resolution of 1°. Thus, the maximum amplitude variation (or ripple) tolerated can be obtained by dividing one time period of the RF signal by 360, $max_{ripple} = 33.613/360 = 0.093\,\text{ps}$.
From Figure 3.24, it appears that the delay amplitude as function of bias voltage follows a non-linear curve. It can also be concluded from Figure 3.24 that the increase in the bias voltage not only increases the delay amplitude, but also results in a decrease of the resonant frequency, which is inconvenient, since it shifts the frequency range affected by the delay. These aspect are further discussed in chapter 4.

3.5 Resonance Wavelength Tuning

The group delay response of an ORR is dependent on the ring round-trip phase shift. Variations in the round-trip phase result in a shift of the resonant frequency, as referred in 3.3.2. It is therefore essential to be able to tune the resonant frequency of the Delay Unit, since it is a means of calibrating the group delay response to operate in the input signal over the desired bandwidth, which can vary, depending on the application. Furthermore, it is also useful for compensating inconvenient frequency shifts that may occur, e.g., from amplitude tuning, as described in the previous section.

3.5.1 Design and Validation

A 100 µm thermo-optic phase shifter section was added to the ring loop, which induces a varying phase shift, governed by the electric current supplied to heat the waveguide. In order to improve the circuit symmetry and to avoid the use of 180° bend waveguides to connect the phase shifter to the variable coupler in the final layout, which would render higher bend losses, two 100 µm waveguide sections were added, as is shown in Figure 3.26. From this stage on, the circuit device will be described as a Delay Unit, since it should already perform the basic functions specified in 3.2. In order to validate the frequency tuning behaviour, a set of bias voltage points were simulated and the respective group delay resonance frequencies were measured. It should be noted that for each bias point simulated, there are multiple resonant frequencies, due to the periodic delay response. The results presented in Table 3.3 correspond to the resonant frequency closest to the operational optical wavelength $\lambda = 1550\,\text{nm}$. For this set of simulations the voltage bias of the variable coupler's phase shifter (which governs the delay amplitude) was kept at $v_{bias1} = 20\,\text{V}$ and only the bias voltage of the ring loop phase shifter was varied $v_{bias2} \in [0;30]V$. The group delay response was also plotted, as illustrated in Figure 3.26. According to the results in Table 3.3, the delay unit is capable of a maximum frequency shift of $\Delta_f = 193.414 - 193.13\,THz = 401GHz$, which greatly exceeds the requirements for this project. Furthermore, because the maximum frequency shift range is larger than the FSR, this means that the group delay curve can be tuned to virtually any frequency (due to the delay's periodic response, there is always another peak within an FSR frequency shift).

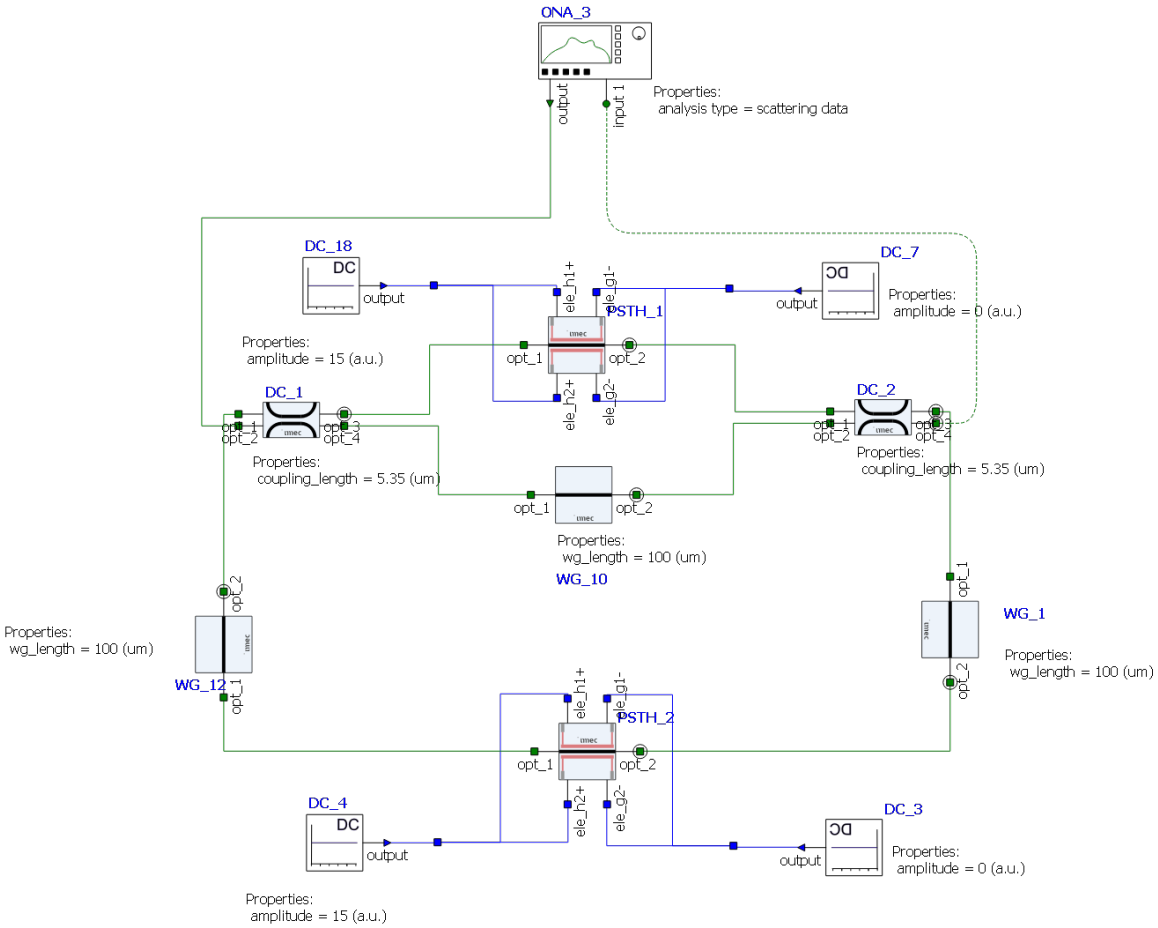

Figure 3.25: Delay unit with resonance frequency tuning

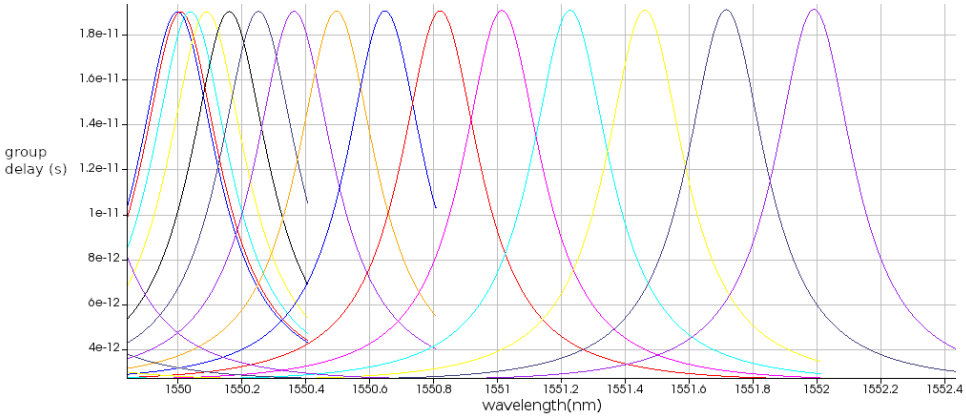

Figure 3.26: Plot of group delay response as a function of ring phase shifter bias voltage

It should be noted that there is a slight variation in amplitude that results from the bias voltage variation, which is $\Delta_{delay} = 19.1696 - 19.035 = 0.1346ps$ for a maximum bias voltage

Bias Voltage (V)	Resonance freq. (THz)	delay (ps)
0	193.414	19.035
2	193.413	19.036
4	193.409	19.038
6	193.403	19.041
8	193.395	19.045
10	193.383	19.051
12	193.370	19.057
14	193.353	19.064
16	193.333	19.074
18	193.312	19.081
20	193.289	19.091
22	193.261	19.106
24	193.232	19.121
26	193.200	19.130
28	193.166	19.147
30	193.130	19.170

Table 3.3: Resonant frequency as a function of ring phase shifter bias voltage

variation. Although not ideal, this factor can be neglected as the application envisaged requires frequency shifts that are considerably smaller and, thus, the amplitude variation that may result is inferior to the maximum acceptable ripple of 0.093 ps.

3.5.2 Delay Bandwidth

The input RF signal has a 500 MHz bandwidth. As a consequence, the delay unit should induce a flat delay over the signal bandwidth, in order to apply a true time delay, that is independent of frequency and thus, eliminates beamsquint in broadband signals [18].
It is, therefore, important to provide a definition for the delay bandwidth. For a delay unit, the *delay bandwidth* will be defined as: *the range of frequencies for which the induced delay (in a specific biasing point) has a ripple lower than* 0.093 ps. As stated in 3.4.2, the peak width decreases for higher peak values, which means that the delay bandwidth decreases for higher delay peak amplitudes. The group delay bandwidth was calculated for a set of delay amplitudes, by varying the coupler bias voltage [4], as shown in table 3.4. The delay amplitudes are actually higher for the same bias voltages than the results of section 3.4.2, because the ring length is higher in this schematic, namely $L = 400 + 2 \cdot 5,35 = 410.7\,\mu m$. As expected, the delay bandwidth decreases with the increase in delay amplitude. The results indicate that a delay unit made up of one ORR can induce a delay with the minimum required bandwidth of

[4]For this set of simulations, the bias voltage of the ring phase shifter was set to 0 V and the coupler bias voltage was varied.

Bias Voltage (V)	Delay Bandwidth (GHz)	Group Delay (ps)
15	13	10.011
17	6	14.728
19	3	24.257
20	2	33.169
20.5	1.8	39.705
21	0.75	48.486
22	0.36	78.482

Table 3.4: Delay Bandwidth

500 MHz for a maximum[5] delay peak amplitude of 48.4886 ps. It follows that the device can supply a delay amplitude range (for the specified bandwidth) of $\Delta_{delay} = 48.486 - 10.011 = 38.475\,ps$, which corresponds to a maximum phase delay of 2.29π for a 29.75 GHz RF signal, which is higher than the minimum 2π delay span required, see 3.2.

3.6 Bend Waveguide

In order to improve the simulation accuracy of the delay unit circuit schematic designed and tested in *Interconnect*, the bends required for the connections between the straight waveguide sections in the ring and between the ring and the directional couplers were designed and properly simulated. Since there is no bend waveguide component block available in the PDK library for Interconnect, a new component had to be designed from scratch. Firstly, the bend 3D model was designed in *FDTD*, which is a simulation program that enables design and simulation of 3D components using the Finite Difference Time Domain method [36]. The bend 3D model is depicted in Figure 3.27. It consists of a 90° bend silicon layer, with a 10 µm radius, 480 nm width and 220 nm height and a silicon oxide cladding layer[6]. Figure 3.28 depicts FDTD simulation results of the intensity of the E-field as it travels through the bend. It can be observed that the optical power is well contained over the bend waveguide.

3.6.1 Bend Losses

The bend model was simulated for the two main sources that contribute to losses of a waveguide,i.e., the propagation losses of the fundamental TE mode and the overlap mismatch losses, which occur at the transition between a straight and bend waveguide [37]. The results obtained are listed below:

- Propagation loss of fundamental TE mode: $4.4906 \cdot 10^{-7}$ dB/cm

[5] Actually it is not the maximum amplitude, it depends on the bias voltage precision. For a bias voltage of 21 V, the delay bandwidth has an extra margin of 250 MHz, or 50%, so slightly higher biasing points are still acceptable, e.g, 21.2V

[6] The actual model has a silicon oxide layer above the silicon layer (red layer), but, in order to capture the silicon layer bend, this top layer was disabled.

Figure 3.27: Bend 3D model

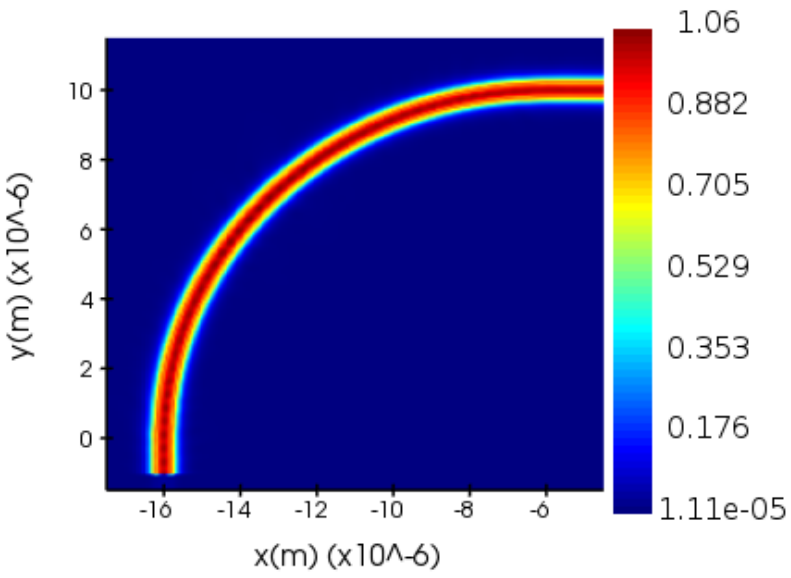

Figure 3.28: E-field intensity

- The overlap between the straight and bend modes (for fundamental TE): 99.9%

Due to the large bend radius, the propagation losses are considerably small. The total loss of the structure can be obtained by adding the contributions of the propagation loss over the bend waveguide length and the mode overlap mismatch at the two interfaces between the

curved and the two straight waveguide sections as follows [37]:

$$Loss = -2 \times 10 \log(0.999)\,[\text{dB}] + (10^{-3}[\text{cm}] \times \frac{\pi}{2})(4.4906 \cdot 10^{-7})\,[\text{dB/cm}] = 0.0087\,\text{dB} \quad (3.8)$$

3.6.2 Validation

The 3D model S-matrix was imported as an Interconnect block and added to the delay unit schematic, as illustrated in Figure 3.29. The schematic was simulated for group delay response, as described in the two previous sections, which rendered similar results, with a slight decrease in delay amplitude and shift in frequency for the respective biasing points. The schematic in Figure 3.29 constitutes the final design of the delay unit.

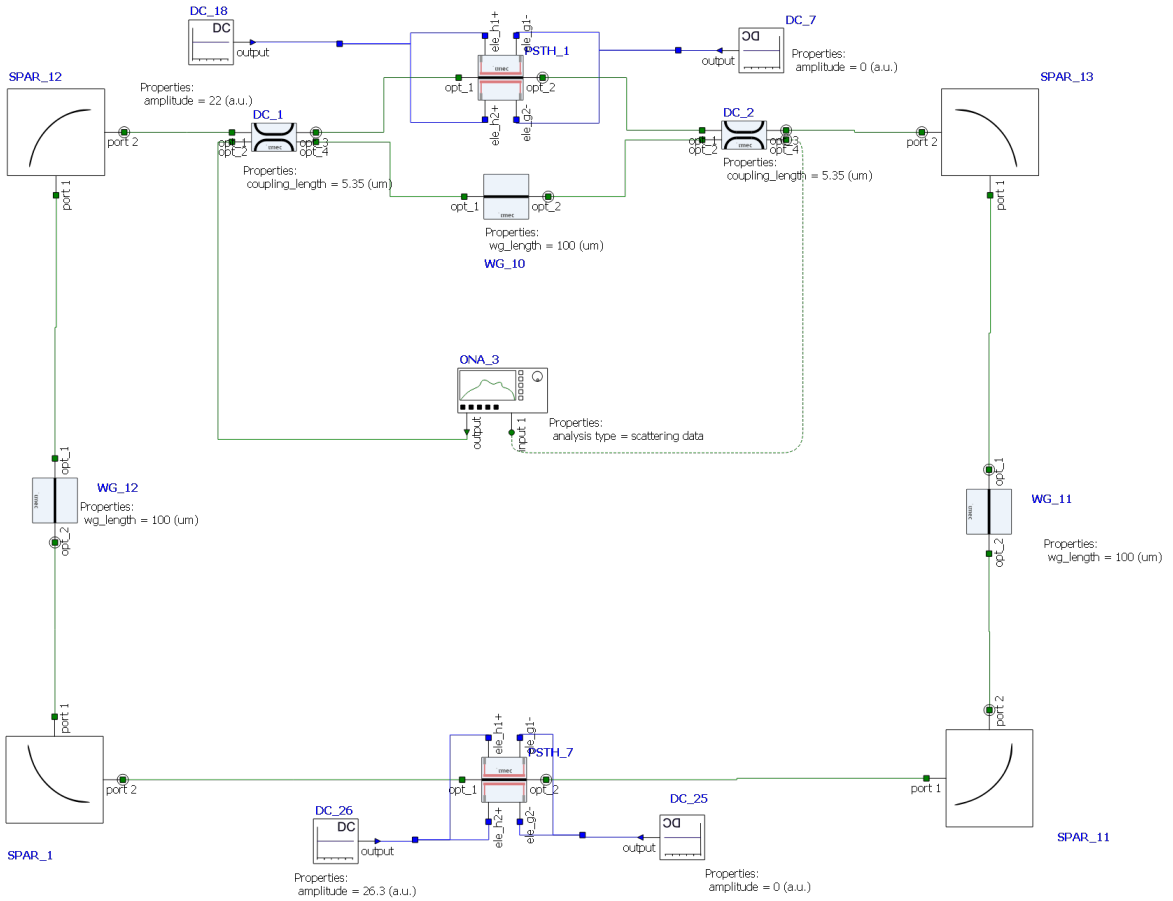

Figure 3.29: Delay Unit schematic with bends

3.7 Summary

In this chapter, a detailed description of the Delay Unit design process was provided. Firstly, the device specifications were outlined. Furthermore, the design approaches executed in order

to meet the specified requirements were characterised, both with theoretical models as well as with simulation results.

Chapter 4

Numerical Simulations

4.1 Introduction

The present chapter contains a detailed account of all relevant numerical simulations performed to the Delay Unit. Section 4.2 presents a full characterisation of the group delay response of the Delay Unit as a function of the input bias voltages and other device constraints. Furthermore, it contains a description of the calibration process of the device, i.e., the process that a Delay Unit controller should execute, in order to calibrate the group delay response to operate in the input signal over the desired bandwidth.
Finally, Section 4.3 describes the set of simulations realised, as a means to validate the Delay Unit performance in a scenario that best approximates an experimental setting.

4.2 Delay Unit Simulation Results

The present section contains an analysis of simulation results concerning the Delay Unit and further characterisation of this device.
The Delay Unit enables the tuning of two main parameters: the group delay amplitude (peak amplitude) and the group delay response resonance frequency. The former parameter is controlled by the bias voltage applied to the phase shifter in the variable coupler and the latter is governed by the bias voltage applied to the ring loop phase shifter. For more details concerning the circuit design and analysis, see chapter 3. As a result, the Delay Unit can be modelled as a function that takes two inputs, i.e., the biasing voltages, and returns an output, i.e, the group delay response, which can be defined by two variables, namely, the group delay peak amplitude and the frequency where that peak occurs [1].
For simplicity of notation, the bias voltage of the variable coupler will be referred to as *Bias Voltage 1* or simply *V1* and the bias voltage of the loop phase shifter will be referred as *Bias Voltage 2* or *V2*. Table 4.1 contains the results of a set of simulations where *V2* was

[1] It should be noted that there are multiple resonant frequencies and multiple peaks, but the analysis is identical for all peaks, due to the periodicity of the group delay response.

set to 0 V and *V1* was tuned at different biasing points. It can be observed in Figure 4.1 that the expected amplitude variation occurs for a variation of *V1*, which appears to follow an exponential curve. Furthermore, Figure 4.2 shows the inconvenient variation in resonance frequency, which needs to be compensated by tuning *V2*.

Bias Voltage 1 (V)	peak delay amplitude (ps)	Resonance Frequency (THz)
15	10.197	193.402
16	12.155	193.400
17	14.881	193.397
18	18.631	193.393
19	24.270	193.391
20	33.165	193.387
21	48.478	193.383
22	78.645	193.380
23	151.961	193.376
23.5	237.917	193.373
24	438.152	193.372

Table 4.1: Group Delay response as function of V1

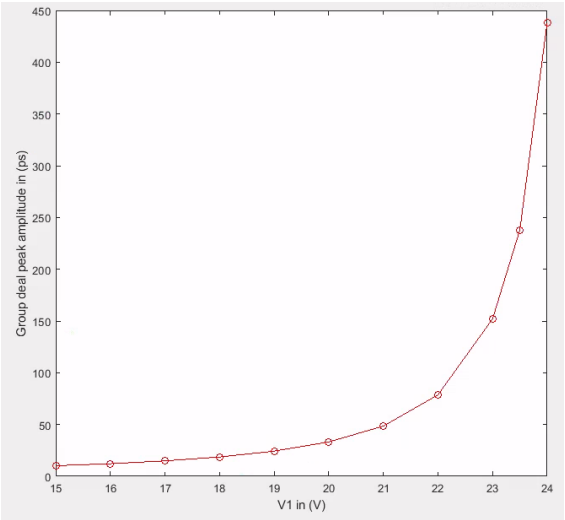

Figure 4.1: Amplitude as a function of V1

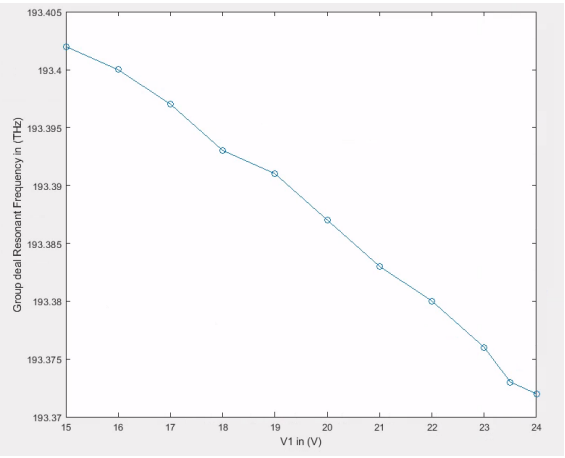

Figure 4.2: Resonance Frequency as a function of V1

Likewise, Table 4.2 contains the simulation results of the Delay Unit group response when only *V2* is tuned and *V1* is set to 18.2 V. As illustrated in Figure 4.3, the resonance frequency is controlled by the variation in V2, following a curve which appears to be polynomial with negative slope. The variation in amplitude, although negligible, as explained in section 3.5, is depicted in Figure 4.4.

Bias Voltage 2 (V)	Resonance freq. (THz)	peak delay (ps)
0	193.414	19.035
2	193.413	19.036
4	193.409	19.038
6	193.403	19.041
8	193.395	19.045
10	193.383	19.051
12	193.370	19.057
14	193.353	19.064
16	193.333	19.074
18	193.312	19.081
20	193.289	19.091
22	193.261	19.106
24	193.232	19.121
26	193.200	19.130
28	193.166	19.147
30	193.130	19.170

Table 4.2: Resonant frequency and delay amplitude as a function of V2

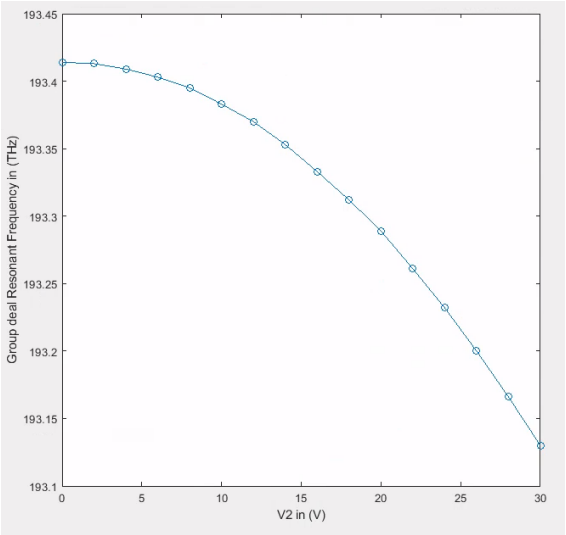

Figure 4.3: Resonance Frequency as a function of V2

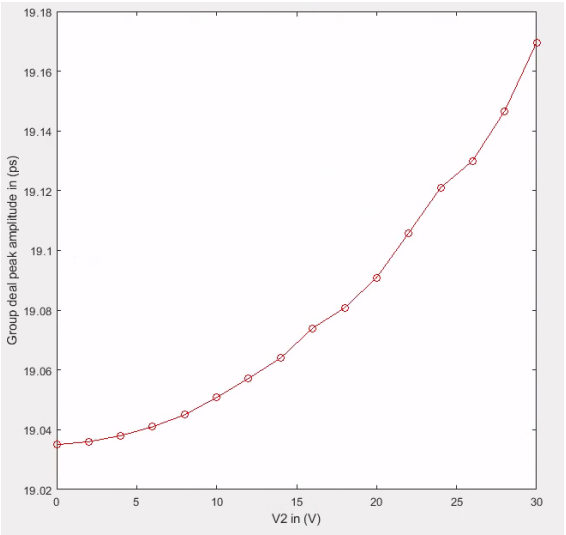

Figure 4.4: Amplitude as a function of V2

According to the Delay Unit response as a function of the two inputs *V1* and *V2* just described, a calibration process was devised that should be followed by the Delay Unit controller:

1. Define a delay amplitude τ to apply to the input optical signal.
2. Define a frequency f for which the delay peak should be applied, i.e., define where the resonance frequency should occur $f_{resonance} = f$.

3. Apply the *V1* value that outputs the delay amplitude defined, τ.

4. Apply the *V2* value that aligns the resonance frequency.

Let us consider an example, where the input optical signal is centred at $f = 193.444\,\text{THz}$ and has a Bandwidth of 500 MHz. Table 4.3 contains a set of Delay Unit simulations for different delays, which were obtained by following the proposed calibration process. Thus, the Delay Unit was calibrated for generating a series of incremental delays and apply them to a signal centred at $f = 193.444\,\text{THz}$. This table contains the biasing points (control input voltages *V1* and *V2*), the delay response parameters (amplitude and resonance frequency) and the phase shift for $f = 193.444\,\text{THz}$, that results from a variation in delay amplitude, relative to a reference delay, e.g., a relative delay variation of $\Delta_\tau = 33.6\,\text{ps}$ corresponds to a 2π phase shift.

V1 (V)	V2 (V)	peak delay amplitude (ps)	Phase delay (radians)
16	25.3	10.9567	0 (reference)
17.6	24.8	15.1755	$\pi/4$
18	24.6	16.6599	1.066
18.6	24.3	19.3751	$\pi/2$
19.3	24.1	23.5567	$3\pi/4$
19.8	23.9	27.4863	π
20.57	23.53	35.8684	$3\pi/2$
21	23.35	42.3623	5.87
21.1	23.3	44.4807	2π

Table 4.3: Use Case example for input signal centred at $f = 193.444\,\text{THz}$

It should be noted that all delay levels presented in Table 4.3 have a delay bandwidth higher than 500 MHz. The biasing points of *V1* and *V2* were obtained by trial and error simulations. In order to facilitate the calibration process, the curves of delay amplitude as a function of *V1* and *V2* were approximated by a polynomial function. Figures 4.5 and 4.6 depict the delay amplitude centred at $f = 193.444\,\text{THz}$ as a function of *V1* and *V2*, respectively, and the polynomial function used to interpolated the points obtained from simulations.

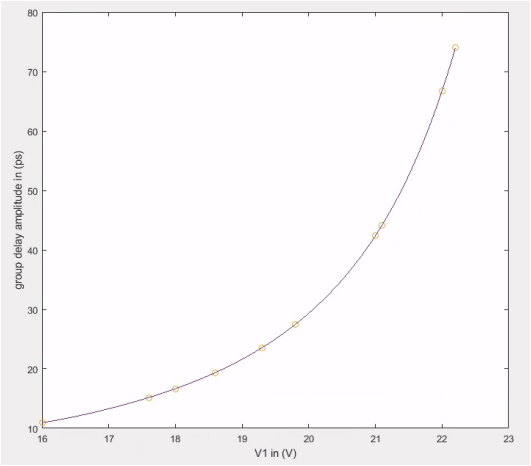

Figure 4.5: Amplitude as a function of V1 + polynomial approximation

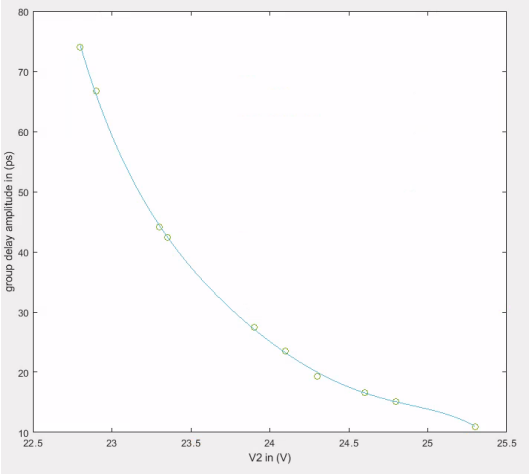

Figure 4.6: Amplitude as a function of V2 + polynomial approximation

The approximations have a correlation of determination higher than (square of the correlation coefficient) $R^2 > 0.9989$. The approximation polynomials provide analytical functions that allow the computation of the delay amplitude (τ) as a function of the bias voltages (v_1 and v_2), without having to resort to trial and error simulations. The polynomial functions obtained are described by the following expressions:

$$\tau = 0.4 \cdot v_1^3 - 24 \cdot v_1^2 - 4 \cdot 10^2 \cdot v_1 + 2 \cdot 10^3 \tag{4.1}$$

$$\tau = -5 \cdot v_2^3 + 4 \cdot 10^2 \cdot v_2^2 - 1 \cdot 10^4 \cdot v_2 + 8 \cdot 10^4 \tag{4.2}$$

Finally, it should be noted that for a minimum delay amplitude resolution of 0.093 ps, the bias voltage supplier must have a resolution of at least 4 mV.

4.3 Modulation and Demodulation

With the Delay Unit's response properly simulated and characterised, the device was tested in a simulation environment that was intended to replicate the conditions of a real application. Accordingly, an optical carrier was generated and modulated by an RF signal, which was fed into the Delay Unit and subsequently converted back to the electric domain by means of a photodetector. Thus, the aim of this testing stage was to check the final electric signal and validate whether the time delays were being correctly applied and, otherwise, to understand what improvements or corrections were necessary.

4.3.1 Intensity Modulation

The modulation technique used in the validation simulations was based on a *Mach-Zender Modulator*, which consists of an MZI with a phase shifter in one of the arms. The MZM

modulates the optical signal intensity, by means of a voltage applied to a phase shifter that induces phase delays in the signal propagating in one of the arms of the MZM which interferes destructively or constructively, when coupled with the signal in the other arm. The output intensity as a function of the induced phase shift follows a cosine squared relation, as explained in section 2.3.4 .

Thus, it is firstly necessary to find the proper biasing point of the MZM, such that a modulation can occur, as linearly as possible. A sweep in the phase shifter bias voltage was performed and the output signal power was measured, in order to determine the optimal biasing point. Figure 4.7 depicts the results of the bias voltage sweep. It is important to mention that these results were obtained for an optical signal operating at a wavelength of $\lambda = 1550\,\text{nm}$ or a frequency of $f = 193.414\,\text{THz}$, because the MZM response will vary with the signal frequency, as demonstrated in the next section 4.3.2. It can be observed from Figure 4.7 that the optimal biasing point should be around $v_{bias} = -2.5\,\text{V}$, for which the modulation signal can have a maximum amplitude of approximately $\pm 1.5\,\text{V}$. The MZM was validated by applying a sine

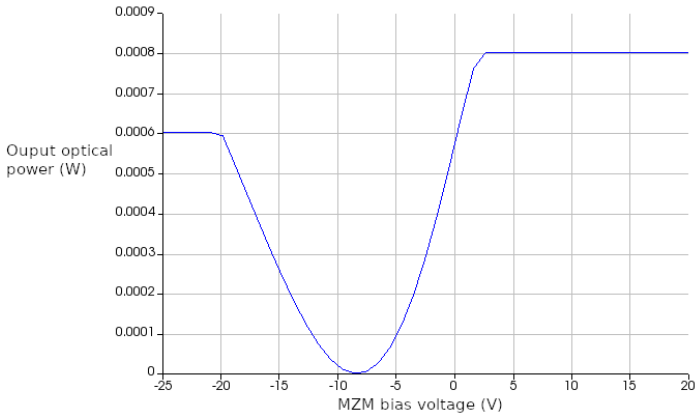

Figure 4.7: MZM response to bias voltage sweep

wave at the phase shifter bias input as shown in Figure 4.8, which yielded, as expected, a sine wave optical signal as illustrated in Figure 4.9. Since the optical intensity is proportional to the square of the optical field, even perfectly linear Intensity Modulation would result in an optical field that has a square-root dependence on the modulating signal. As a consequence, the optical spectrum at the output of the MZM would consist of the optical carrier frequency line and an infinite number of sidebands, with a number of significant sidebands that increase with the increase in modulation depth [13]. Therefore, the modulation depth should be minimised such that only the first order sidebands are relevant, which means that the Delay Unit should be designed in order to apply a flat delay to the optical carrier and the first two sidebands, as illustrated in Figure 4.10. Due to this requirement, a test signal with a frequency of 2 GHz was used, so as to minimise the delay bandwidth required (which is equal to 4 GHz) and thus minimising the Delay Unit complexity. Moreover, the modulating signal has a low amplitude of 0.75 V, so as to minimise the modulation depth. In order to meet

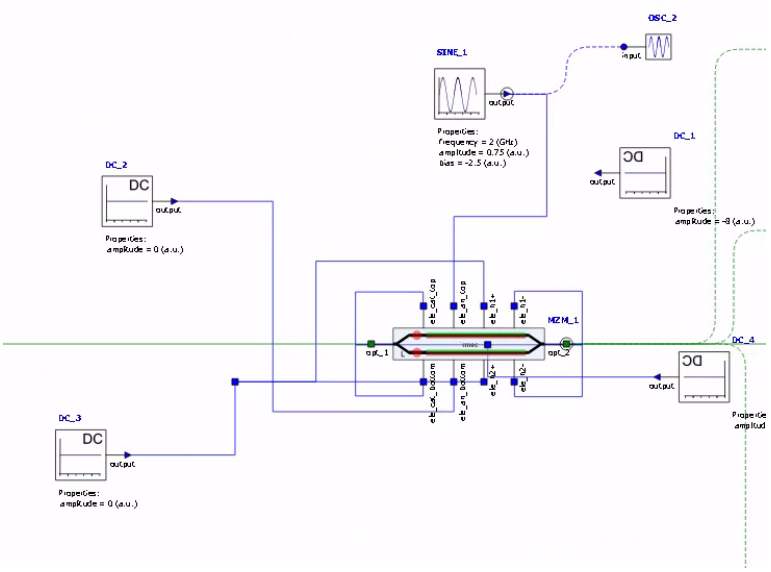

Figure 4.8: MZM schematic

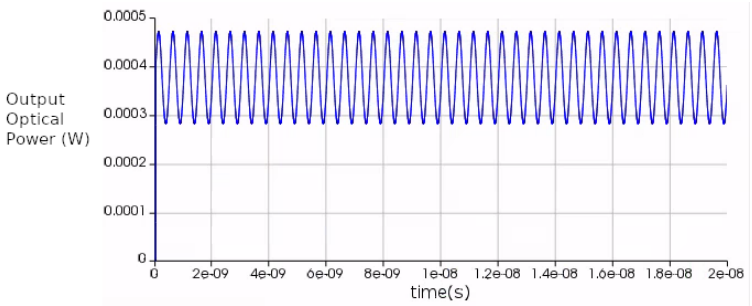

Figure 4.9: MZM output signal

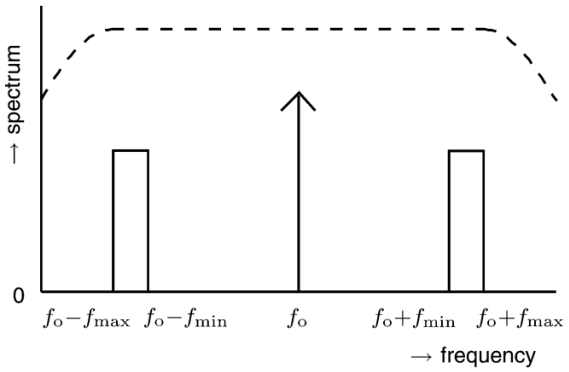

Figure 4.10: Spectrum of modulated signal. The dotted line describes the necessary delay bandwidth [13].

the bandwidth requirements, the Delay Unit was made up of two rings connected in series, as depicted in Figure 4.11, which increase the flat delay bandwidth as evidenced by Figure

4.12. A set of bias points were determined with trial-and-error simulation by calibrating the

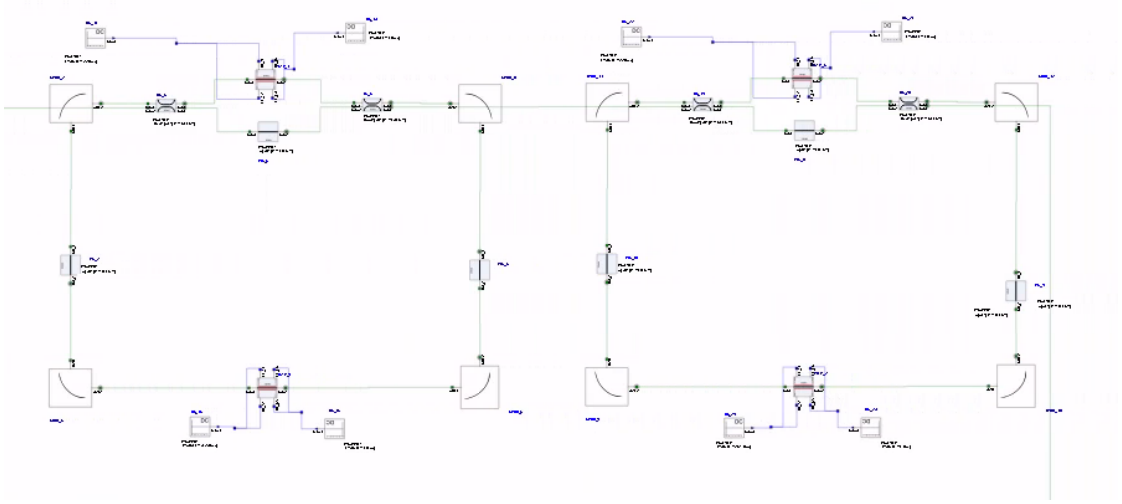

Figure 4.11: Delay Unit with two cascaded rings

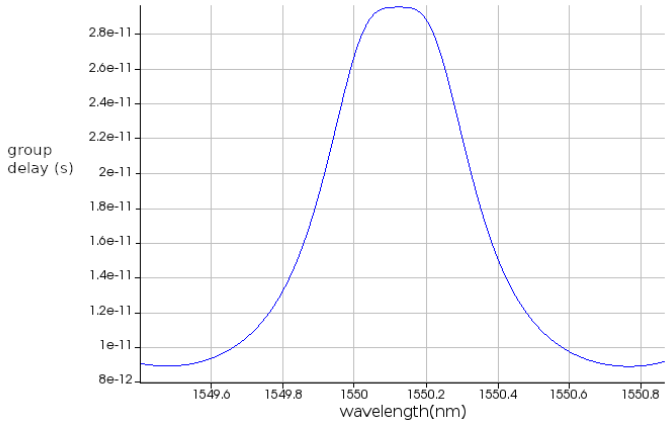

Figure 4.12: Delay Unit response

Delay Unit for increasing delay amplitudes centred at 193.414 THz as illustrated in Table 4.4. It should be noted that, in this case there are 4 input variables, because there are two ORR in the Delay Unit.

V1 ORR1 (V)	V2 ORR1 (V)	V1 ORR2 (V)	V2 ORR2 (V)	Delay Ampl. (ps)
16	30	16	25.3	17.8
20	27.5	20	26	42.3
22	26.3	22	25.6	92.6
23	25.9	23	25.4	147
23.5	25.6	23.5	25.2	202.5

Table 4.4: Biasing points for a 2 ORR Delay Unit with increasing delays centred at 193.414 THz

The MZM was connected to the Delay Unit, which was connected to a photodetector, with a spectrum analyser and an electric oscilloscope at the photodetector output. Despite the good results in the MZM and Delay Unit Response, the electric signal obtained after the photodetector did not yield the expected delay results. Not only the relative delays between the electric signals did not match the expected delays induced by the Delay Unit, but the signal suffered considerable distortion, as evidenced by Figure 4.13, which depicts the electric signals for the different delay levels.

These inconsistencies may be a consequence of the distortion caused by the higher order

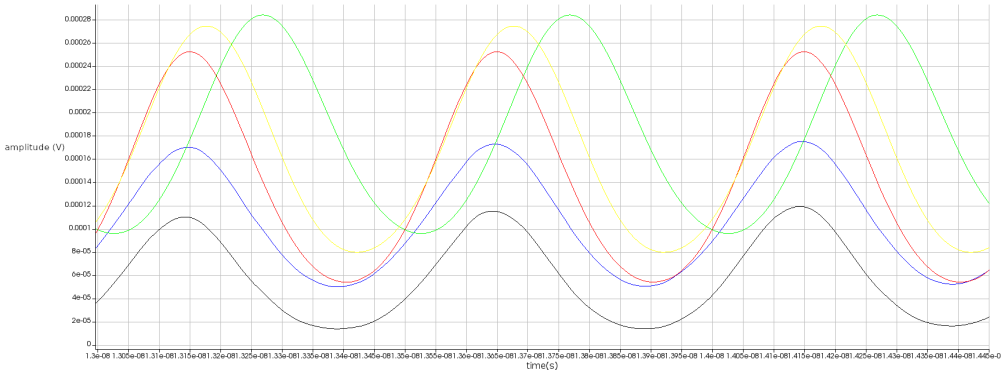

Figure 4.13: Electric signals after photodetector demodulation

sidebands which are not affected by the Delay Unit. The photodetector response can also be responsible for this phenomenon. Furthermore, the spectrum of the intensity-modulated signal is highly dependent on the modulation method and modulation parameters, such as the modulation depth. In chapter 6, the realisation of tests using coherent optical modulation is suggested as future work, which might overcome some of the issues outlined in this section.

4.3.2 Single-Sideband Suppressed Carrier Modulation

An alternative to simple Intensity Modulation is suggested by [13], in which the optical carrier is suppressed, along with the lower sideband. This method is referred to as Single-Sideband Suppressed Carrier Modulation, or SSB-SC. An advantage of this method is that it requires a lower delay bandwidth and, thus, a less complex Delay Unit circuit. Figure 4.3.2 depicts the optical signal spectrum at the output of the MZM and the required flat delay bandwidth.

Because the delay only needs to be applied to one sideband, the Delay Unit requires only one ORR. Furthermore, an RF signal with frequency 29.75 GHz was used, in order to better replicate the application intended for this project. It should be noted that the modulating signal used consists of a simple sine wave, because it is easier to observe the phase shifts on the oscilloscope. However, for the real application, an RF signal with 500 MHz would be used to modulate the optical carrier.

The carrier and sideband suppression is performed by means of an optical band-pass filter, with a pass band configured to the upper sideband of the modulated signal, as illustrated

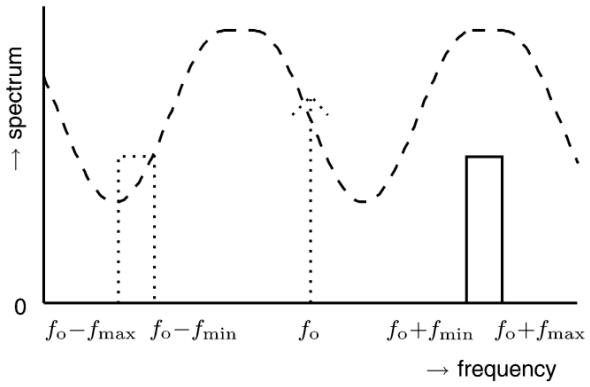

Figure 4.14: Spectrum of modulated signal after carrier and sideband suppression. The dotted line describes the necessary delay bandwidth [13].

in Figure 4.15, which is $f_{SB} = 193.414\,\text{THz} + 30\,\text{GHz} = 193.444\,\text{THz}$. After the SSB-SC modulation, the single sideband optical signal is connected to the Delay Unit. The output signal of the Delay Unit is combined with the optical carrier and subsequently connected the photodetector. It should be noted that the optical carrier is split in two beams after the laser: one is fed into the MZM and the other is combined with the output signal of the Delay Unit, as shown in Figure 4.16.

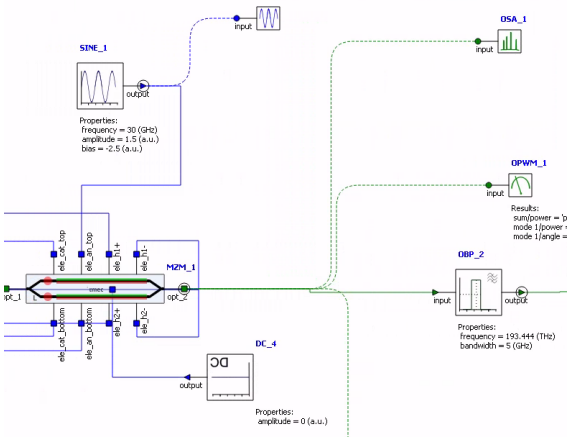

Figure 4.15: MZM based Intensity Modulation with SSB-SC

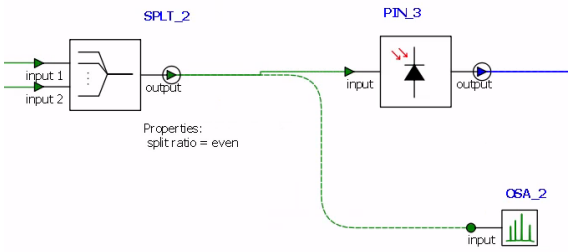

Figure 4.16: Before the photodetector, the Delay Unit output is combined with the optical carrier

The Delay Unit was calibrated to centre the group delay response at 193.444 THz. The delay amplitude levels tested are depicted in Table 4.5. The schematic was simulated for each delay level and the electric signals after the detection were plotted with the oscilloscope, in order to observe the relative phase shifts between the resulting signals for each delay level described in Table 4.5. Some promising results were obtained, however the *Bias Voltage 2* had to be modified. Furthermore, the phase shifts only matched the expected results from 0 to π, for higher delays the results were not conclusive. Figure 4.17 depicts the relative phase shifts

V1 (V)	V2 (V)	peak delay amplitude (ps)	Phase delay (radians)
16	25.3	10.9567	0 (reference)
17.6	24.8	15.1755	$\pi/4$
18.6	24.3	19.3751	$\pi/2$
19.3	24.1	23.5567	$3\pi/4$
19.8	23.9	27.4863	π
20.57	23.53	35.8684	$3\pi/2$
21.1	23.3	44.4807	2π

Table 4.5: Group Delay levels simulated and corresponding biasing points for $f = 193.444\,\text{THz}$

between the electric signals, for induced delay levels corresponding to $0, \pi/4, \pi/2, 3\pi/4, \pi$.

Although SSB-SC modulation yielded some improvements over simple Intensity Modulation,

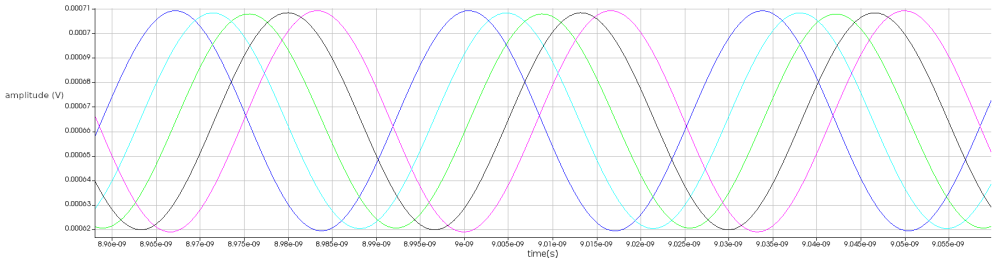

Figure 4.17: Electric signals after the photodetector detected by the oscilloscope

the results were not fully consistent with the Delay Unit response. These inconsistencies may be a consequence of a phase shift mismatch between the carrier and the sideband, which can lead to distortions generated by the photodetector. Furthermore, changing the modulation method, e.g., by using coherent modulation, might eliminate some of the inconsistencies in the simulation results.

4.4 Summary

In this chapter the Delay Unit was subjected to multiple numerical simulations, in order to characterise with detail the group delay response, as well as to validate the device performance in a scenario that best approximates an experimental setting. The Delay Unit response was properly characterised and some analytical models were developed, as a means of extrapolating the complete device response from a set of finite simulation results. The validation set of simulations described in section 4.3 yielded promising results, but also some inconsistencies between the simulation results and the expected Delay Unit response were observed.

Chapter 5

Beamformer

5.1 Introduction

This chapter presents the overall optical beamformer architecture. Section 5.2 provides a description of the Phased Array Antenna model envisaged for the proposed application, which determines the beamformer architecture specifications. Section 5.3 outlines the system architecture and Section 5.4 describes the implementation of the optical beamformer in a Silicon Photonic Chip Layout.

5.2 Array Antenna

5.2.1 Linear Array Model

The proposed PIC beamformer was developed for a 1×4 linear broadside array antenna. The array should be designed to operate at $f = 29.75\,\text{GHz}$, for a broadband RF signal with a 500 MHz bandwidth. The array is made up of four stationary antenna elements, equally distanced by $d = \lambda/4$, where $\lambda = \frac{c}{29.75\,\text{GHz}} \approx 1\,\text{cm}$ is the operation wavelength. Figure 5.1 depicts a diagram of the array antenna. This element separation value was chosen so that there would be no principal maxima (*main lobes*) in other directions, which are referred to as *grating lobes* [1].
It should be noted that a beamformer usually controls the amplitude a_i and phase φ_i of an Antenna Element. Tuning the AE signal amplitude can affect the beam shape, by changing the beam pattern lobes amplitude and position; whereas the change in phase can affect the beam direction [16] [31]. For this project, a particular case of sheer beam steering was considered, where $a_i = a1 \,\forall\, 1 \leq i \geq N$ and only the AE phase is variable and set by the beamformer.

5.2.2 Progressive phase shift

The proposed beamformer should be capable of scanning the beam maximum radiation for a total of 60°, i.e., it should allow scanning of ±30° from the default maximum radiation

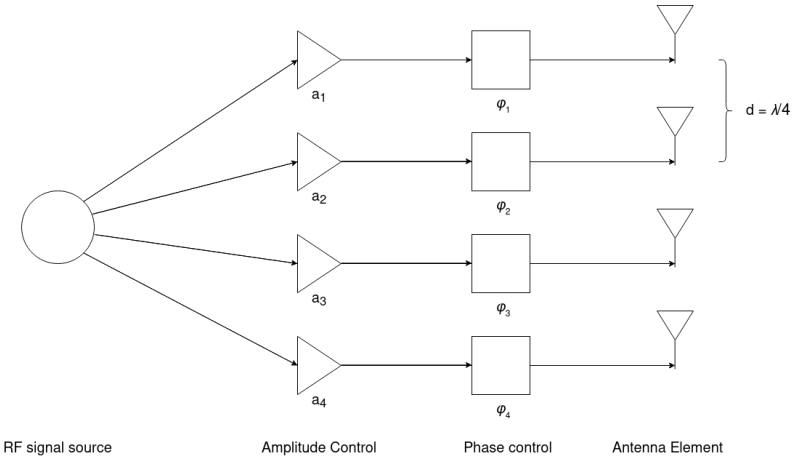

Figure 5.1: Phased Antenna Array Diagram

direction. In this section, the progressive phase shift interval necessary for this beam scanning range will be calculated.

A Broadside Phased Array Antenna was considered for this project. This means that the maximum radiation of the array is directed normal to the axis of the array [1], as illustrated in Figure 5.2.

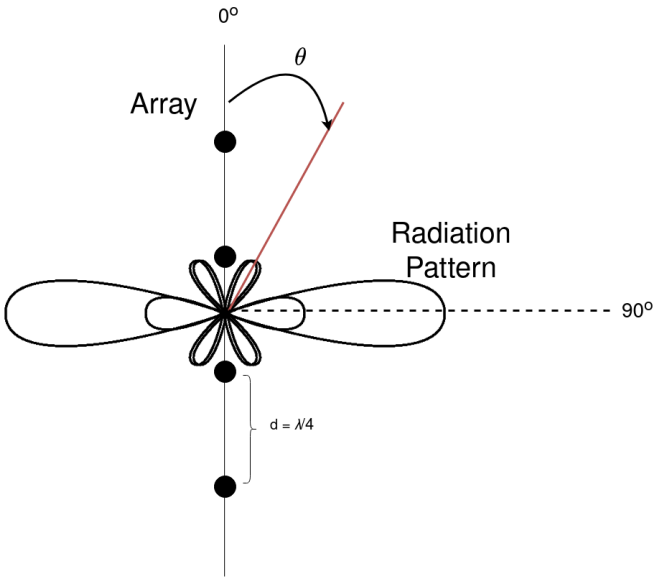

Figure 5.2: Broadside Antenna Array Diagram

As explained in section 2.2.1, the array factor can be described as follows:

$$AF = \frac{\sin(\frac{N}{2}\psi)}{\sin(\frac{1}{2}\psi)} \tag{5.1}$$

which is a 2π periodic function of $\psi = kd\cos\theta + \beta$, where d is the element separation, k is the propagation constant and β is the progressive phase shift, which is defined as the difference in phase on each consecutive pair of AEs: $\beta = \varphi_2 - \varphi_1 = \varphi_3 - \varphi_2 = ... = \varphi_N - \varphi_{N-1}$. From Equation 5.1, it follows that the first maximum of the array factor occurs when:

$$\psi = kd\cos\theta + \beta = 0 \tag{5.2}$$

For a broadside array, the default maximum direction should be normal to the axis of the array [$\theta_{max} = 90$ degree]. Therefore, a 60° scanning range implies scanning the maximum radiation direction from $\theta_{max} = 60°$ to $\theta_{max} = 120°$. The progressive phase shifts for a maximum radiation set to $\theta_{max} = 60°$ and $\theta_{max} = 120°$ are obtained in 5.3 and 5.4, respectively.

$$\psi = kd\cos\theta + \beta|_{\theta=60°} = 0 \Leftrightarrow kd\frac{1}{2} + \beta = 0 \Leftrightarrow \beta = \frac{-\pi d}{\lambda} \tag{5.3}$$

$$\psi = kd\cos\theta + \beta|_{\theta=120°} = 0 \Leftrightarrow -kd\frac{1}{2} + \beta = 0 \Leftrightarrow \beta = \frac{\pi d}{\lambda} \tag{5.4}$$

Thus, for a scanning range from $\theta_{max} = 60°$ to $\theta_{max} = 120°$, the beamformer must generate progressive phase shifts within the interval:

$$\frac{-\pi d}{\lambda} \leq \beta \leq \frac{\pi d}{\lambda} \Leftrightarrow \frac{-\pi}{4} \leq \beta \leq \frac{\pi}{4} \tag{5.5}$$

For a progressive phase shift $\beta = \frac{-\pi}{4}$, a possible set of AE phase delays could be: $\varphi_1 = \frac{3\pi}{4}$; $\varphi_2 = \frac{\pi}{2}$; $\varphi_3 = \frac{\pi}{4}$; $\varphi_4 = 0$. It can be concluded from these results, that the minimum required phase shift range in each AE necessary to meet the beam direction scanning requirements is $[0; \frac{3\pi}{4}]$. Thus, the Delay Unit developed and characterised in Chapters 3 and 4 is suitable for this application, as it is has a total phase shift range of $[0; 2\pi]$.

5.3 System Architecture

From the example in the previous section, it is clear that the phase delay induced for each AE will always be different (except for $\beta = 0$). Thus, the proposed beamformer architecture includes four delay units, one for each AE, as depicted in Figure 5.3. On the left side, an optical carrier is modulated by the input RF signal, which is then split into 4 beams, one for each *Delay Unit*. The delay units are controlled by two electric signals, which are set by a controller, which calculates the required voltage inputs for a specific delay, referred to as *Control Unit* [1]. After passing through the delay unit, the optical signal is subsequently demodulated using a *Photo-Detection System* and the resulting RF signal is fed into the AE. The dotted line denotes the section of the beamformer which was integrated into a Silicon Photonic Chip.

[1] The design of the control unit is out of the scope of this project.

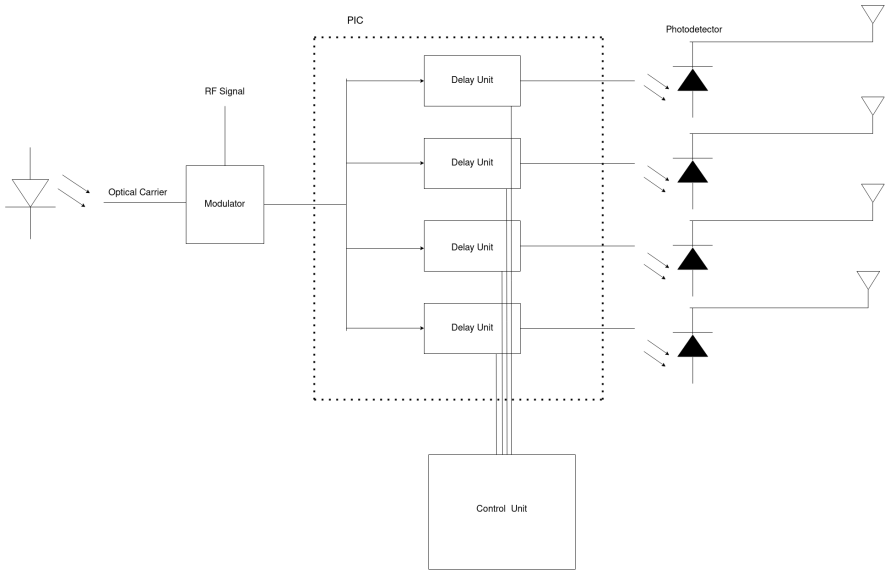

Figure 5.3: Beamformer Architecture Diagram

5.4 Layout Development

The present section presents the layout developed for the proposed Beamformer Photonic Chip. The layout technology PDK was supplied by the *IMEC* foundry and the layout was designed using the *Klayout* software. Figure 5.4 depicts the overall layout. The chip has a size of 5150 µm × 5150 µm.

5.4.1 Input/Output Coupling

The light is coupled to and from the chip by means of a fibre array made up of 8 grating couplers. The grating couplers on the edges are connected together, in order to measure the coupling efficiency and calibrate the optimal position of the I/O fibre array in the chip. This component is depicted in Figure 5.5. In order to eliminate reflections at the I/O coupling section, adiabatic bends are connected to the grating couplers, which redirect possible reflections away from the grating coupler. This is relevant for I/O connections, namely when cavity lasers are used to generate light, which are especially sensitive to reflections [26]. The adiabatic bends used are either a single or double bend, as illustrated in Figures 5.6 and 5.7, respectively. It should be noted that the bends were designed according to the specifications outlined in section 3.6.

5.4.2 Delay Unit

There are 4 delay units, one for each Antenna Element. A single beam of light is coupled into the chip, which is split into 4 beams, with a set of Multi-Mode Interferometers, as depicted in Figure 5.8. This process is necessary, in order to preserve coherence at the input of every

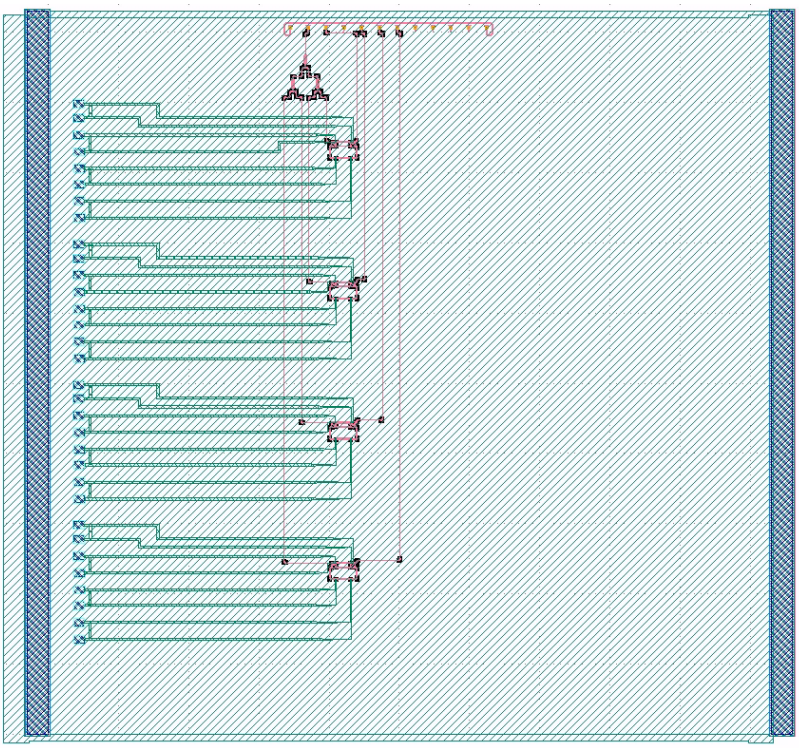

Figure 5.4: Beamformer Photonic Chip Layout

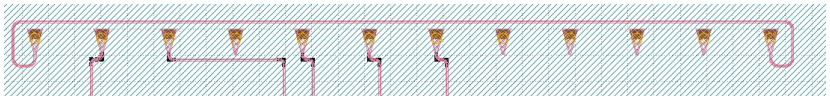

Figure 5.5: Grating Coupler Fibre Array

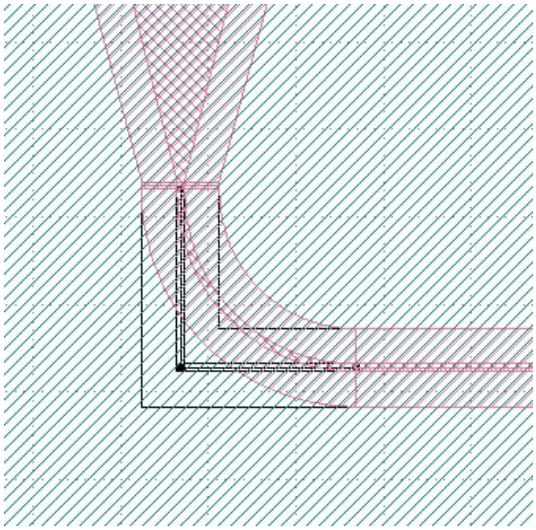

Figure 5.6: Single Adiabatic Bend Layout

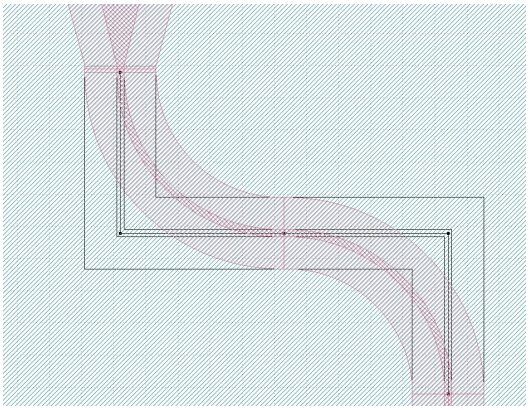

Figure 5.7: Double Adiabatic Bend Layout

delay unit, as opposed to, e.g, generating 4 different input optical signals.
The layout of a delay unit is depicted in Figure 5.9, with the MZI based variable coupler on top that is connected with directional couplers to the ring loop at the bottom. The green layers constitute the electrical connections that feed the electrical current to the phase shifter heaters.

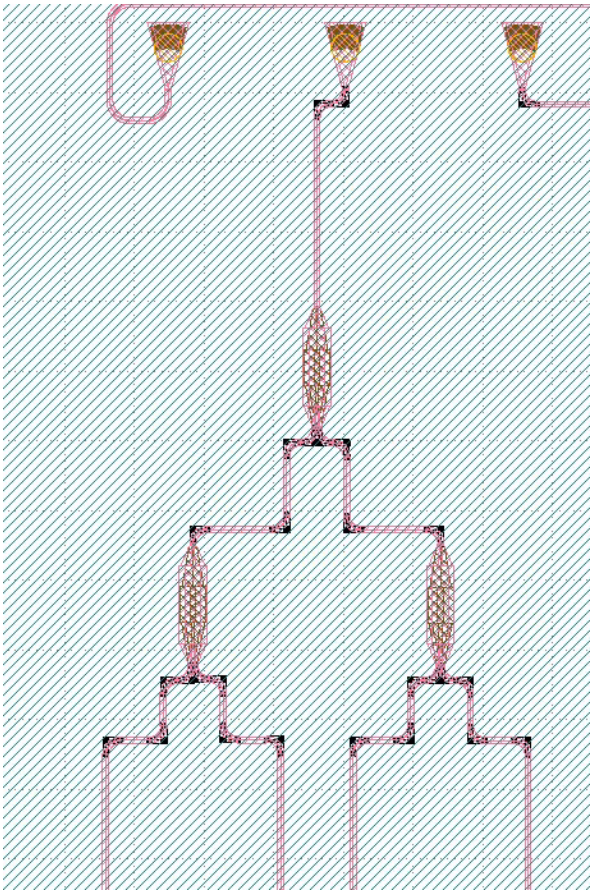

Figure 5.8: MMI 1×4 splitter

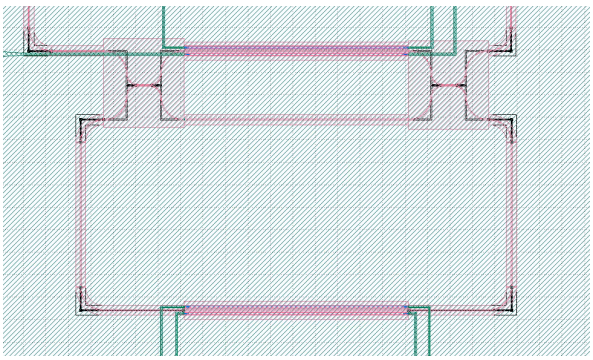

Figure 5.9: Delay Unit Layout

5.4.3 Electric contacts

The *IMEC* PDK phase shifter is comprised of a silicon waveguide and two heaters, one on each side. Each heater has two electric contacts: a positive and a ground connection. Thus, each phase shifter has a total of 4 electrical connections. There are 2 phase shifters per delay unit and 4 delay units in total in the chip, adding up to a total of 32 electrical connections. Since both heaters in each phase shifter have the same applied voltage, the electrical connections are shunt in pairs, near the bondpads, as depicted in Figure 5.10.
Naturally, given the symmetry in the phase shifter structure, the number of bondpads could have been reduced by half, by shunting both "positives" and "grounds", respectively, near the phase shifter and eliminating one of the electrical paths. However, this would increase the total resistance of the electrical connections and, therefore, increase the power consumption of the chip. For the same reason, the electrical layers have a larger width than the electric contacts in the phase shifter, which are connected to the layers with larger width by means of a taper, as illustrated in Figure 5.11.

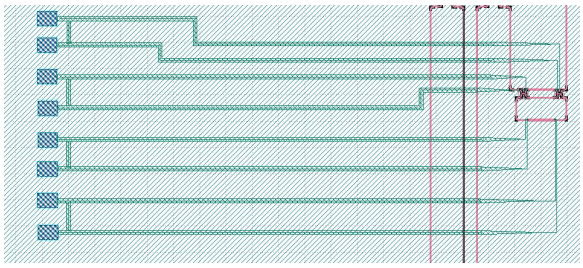

Figure 5.10: Delay Unit Electrical Connections and Bondpads

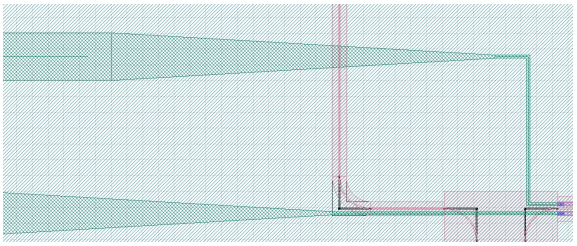

Figure 5.11: Taper Example Layout

5.5 Summary

In this chapter the optical beamformer architecture was outlined. Firstly, the Phased Array Antenna was characterised, which imposed the relevant requirements for the beamformer architecture. Furthermore, the system architecture was defined and, finally, the optical beamformer was properly implemented in a Photonic Integrated Chip layout.

Chapter 6

Final Remarks

6.1 Goal Achievement

This dissertation project had the objective of designing and simulating a beamformer implemented in a PIC that was based in true time delay and that could support broadband signals in Phased Array Antennas.
In order to solve this problem, the beamformer device was decomposed into simpler components, which were carefully studied and designed and then integrated in a photonic chip. The most relevant component designed was the Delay Unit, which consists of an optical circuit that induces flat group delay over a wide frequency range that is fully tunable, both in amplitude and frequency response. These functionalities were addressed by developing a device based on an ORR connected with an MZI variable coupler. Every functional requirement was achieved and validated in simulation, namely:

- A tunable delay range corresponding to a phase shift between 0 and 360°.
- A minimum delay step that provides a phase shift resolution of 1°.
- A flat delay response over a minimum frequency span of 500 MHz.

Subsequently, the Delay Unit was characterised in detail and this device underwent simulations to best replicate a real experimental scenario. These simulations yielded promising results, as well as some discrepancies from the expected behaviour. Nevertheless, these inconsistencies do not stem from the Delay Unit response, which was carefully tested, but from some conditions of the simulation environment developed, such as the modulation method used and phase shift mismatches introduced by other circuit elements.
Finally, the individual components were integrated into a Silicon Photonic Chip in order to form a functional beamformer for a 1×4 linear Phased Array Antenna that is capable of scanning the beam direction over a range of 60°, i.e., ±30° from the normal direction to the array axis.

6.2 Future Work

The main goals proposed for this project were achieved and the work developed and described in this dissertation constitutes a viable solution for the problem outlined in chapter 1. Nevertheless, there is always room for improvement. The following list contains a few suggestions for work to be developed in the future:

- Integrate the Modulation and Demodulation blocks of the beamformer system into the Photonic Chip.
- Investigate the feasibility of altering some of the design features in the variable coupler, in order to shift the usable bias voltage range to lower voltages,and thus decreasing the power consumption of the circuit.
- Implementation of coherent modulation for the Delay Unit simulations. Investigate further into the discrepancies observed and alter the necessary simulation schematic characteristics.
- Chip Fabrication and experimental validation.

Bibliography

[1] C. A. Balanis, *Antenna theory: analysis and design*. John wiley & sons, 2016.

[2] D. M. Pozar, *Microwave engineering*. John wiley & sons, 2011.

[3] W. Rotman and R. Turner, "Wide-angle microwave lens for line source applications," *IEEE Transactions on antennas and propagation*, vol. 11, no. 6, pp. 623–632, 1963.

[4] L. Chrostowski and M. Hochberg, *Silicon photonics design: from devices to systems*. Cambridge University Press, 2015.

[5] C. Pollock and M. Lipson, *Integrated photonics*, vol. 20. Springer, 2003.

[6] C.-L. Chen, *Foundations for guided-wave optics*. John Wiley & Sons, 2006.

[7] M. Izutsu, Y. Nakai, and T. Sueta, "Operation mechanism of the single-mode optical-waveguide y junction," *Optics letters*, vol. 7, no. 3, pp. 136–138, 1982.

[8] C. K. Madsen and J. H. Zhao, *Optical filter design and analysis*. Wiley New York, 1999.

[9] "The talbot-effect, quantum interactive website." https://interactive.quantumnano.at/advanced/quantum-experiments/talbot-effect/. Accessed: 2021-02-09.

[10] L. B. Soldano and E. C. Pennings, "Optical multi-mode interference devices based on self-imaging: principles and applications," *Journal of lightwave technology*, vol. 13, no. 4, pp. 615–627, 1995.

[11] Y. Wang, J. Flueckiger, C. Lin, and L. Chrostowski, "Universal grating coupler design," in *Photonics North 2013*, vol. 8915, p. 89150Y, International Society for Optics and Photonics, 2013.

[12] D. H. Geuzebroek and A. Driessen, "Ring-resonator-based wavelength filters," in *Wavelength filters in fibre optics*, pp. 341–379, Springer, 2006.

[13] A. Meijerink, C. G. Roeloffzen, R. Meijerink, L. Zhuang, D. A. Marpaung, M. J. Bentum, M. Burla, J. Verpoorte, P. Jorna, A. Hulzinga, *et al.*, "Novel ring resonator-based integrated photonic beamformer for broadband phased array receive antennas—part i: Design and performance analysis," *Journal of Lightwave Technology*, vol. 28, no. 1, pp. 3–18, 2009.

[14] C. Roeloffzen, L. Zhuang, R. Heideman, A. Borreman, and W. Van Etten, "Ring resonator-based tunable optical delay line in lpcvd waveguide technology," in *Proc. 9th IEEE/LEOS Symp. Benelux*, pp. 79–82, 2005.

[15] L. Zhuang, C. G. Roeloffzen, M. Hoekman, K.-J. Boller, and A. J. Lowery, "Programmable photonic signal processor chip for radiofrequency applications," *Optica*, vol. 2, no. 10, pp. 854–859, 2015.

[16] R. J. Mailloux, *Phased array antenna handbook*. Artech house, 2017.

[17] R. E. Wallis, J. R. Bruzzi, and P. M. Malouf, "Testing of the messenger spacecraft phased-array antenna," *IEEE Antennas and Propagation Magazine*, vol. 47, no. 1, pp. 204–209, 2005.

[18] R. Rotman, M. Tur, and L. Yaron, "True time delay in phased arrays," *Proceedings of the IEEE*, vol. 104, no. 3, pp. 504–518, 2016.

[19] "Starlink." https://www.starlink.com. Accessed: 2021-02-08.

[20] I. Zand and W. Bogaerts, "Discretization effects of digital control of thermally tunable 2× 2 mzi couplers," in *2019 IEEE Photonics Society Summer Topical Meeting Series (SUM)*, pp. 1–2, IEEE, 2019.

[21] J. McCaulley, V. Donnelly, M. Vernon, and I. Taha, "Temperature dependence of the near-infrared refractive index of silicon, gallium arsenide, and indium phosphide," *Physical Review B*, vol. 49, no. 11, p. 7408, 1994.

[22] H. Shang, D. Sun, P. Yu, B. Wang, T. Yu, T. Li, and H. Jiang, "Investigation for sidewall roughness caused optical scattering loss of silicon-on-insulator waveguides with confocal laser scanning microscopy," *Coatings*, vol. 10, no. 3, p. 236, 2020.

[23] M.-S. Kim, T. Scharf, C. Menzel, C. Rockstuhl, and H. P. Herzig, "Talbot images of wavelength-scale amplitude gratings," *Optics express*, vol. 20, no. 5, pp. 4903–4920, 2012.

[24] W. Bogaerts, P. De Heyn, T. Van Vaerenbergh, K. De Vos, S. Kumar Selvaraja, T. Claes, P. Dumon, P. Bienstman, D. Van Thourhout, and R. Baets, "Silicon microring resonators," *Laser & Photonics Reviews*, vol. 6, no. 1, pp. 47–73, 2012.

[25] "Continuous-wave operation." https://www.rp-photonics.com/continuous_wave_operation.html. Accessed: 2021-02-08.

[26] G. Keiser, *Optical fiber communications*. McGraw Hill, 2010.

[27] M. Cai, O. Painter, and K. J. Vahala, "Observation of critical coupling in a fiber taper to a silica-microsphere whispering-gallery mode system," *Physical review letters*, vol. 85, no. 1, p. 74, 2000.

[28] J. Lee, R. Y. Loo, S. Livingston, V. I. Jones, J. B. Lewis, H.-W. Yen, G. L. Tangonan, and M. Wechsberg, "Photonic wideband array antennas," *IEEE Transactions on Antennas and Propagation*, vol. 43, no. 9, pp. 966–982, 1995.

[29] J. Corral, J. Marti, J. Fuster, and R. Laming, "True time-delay scheme for feeding optically controlled phased-array antennas using chirped-fiber gratings," *IEEE Photonics Technology Letters*, vol. 9, no. 11, pp. 1529–1531, 1997.

[30] S. Blanc, M. Alouini, K. Garenaux, M. Queguiner, and T. Merlet, "Optical multibeamforming network based on wdm and dispersion fiber in receive mode," *IEEE transactions on microwave theory and techniques*, vol. 54, no. 1, pp. 402–411, 2006.

[31] G. Serafino, C. Porzi, B. Hussain, F. Scotti, F. Falconi, M. Chiesa, V. Toccafondo, A. Bogoni, and P. Ghelfi, "High-performance beamforming network based on si-photonics phase shifters for wideband communications and radar applications," *IEEE Journal of Selected Topics in Quantum Electronics*, vol. 26, no. 5, pp. 1–11, 2020.

[32] "Jet talk in-flight-connectivity." http://jet-talk.com/. Accessed: 2021-06-06.

[33] M. Skolnik, "Update to foreign space objects determination: Overview of satellite operators," tech. rep., Australian Communications and Media Authority, 2019.

[34] "Interconnect: Photonic integrated circuit simulator." https://www.lumerical.com/products/interconnect/. Accessed: 2021-06-06.

[35] "Ring resonator using interconnect primitive elements." https://support.lumerical.com/hc/en-us/articles/360042323794-Ring-resonator-using-INTERCONNECT-primitive-element Accessed: 2021-06-06.

[36] "Lumerical, finite difference time domain (fdtd) solver." https://support.lumerical.com/hc/en-us/articles/360034914633-Finite-Difference-Time-Domain-FDTD-solver-introduct Accessed: 2021-06-06.

[37] "Bent waveguide analysis." https://support.lumerical.com/hc/en-us/articles/360042799933-Bent-waveguide-analysis. Accessed: 2021-06-06.